A Role for the Ocean in the Winter Sea Ice Distribution North of Svalbard

Christophe Herbaut, Marie-Noëlle Houssais, Anne-Cécile Blaizot, Jean-Marc Molines

A role for the ocean in the winter sea ice distribution north of Svalbard.

Christophe Herbaut[1], Marie-Noëlle Houssais[1], Anne-Cécile Blaizot[1] and Jean-Marc Molines[2]

1 : LOCEAN, Sorbonne Université, CNRS, IRD, MNHN

2 : Institut des Géosciences de l'Environnement, Université Grenoble-Alpes, CNRS

Key Points:

- Identification of large ice melt rates in pack ice along the pathway of the Atlantic Water.
- Two main types of large melt events: a) ice advection over warm SST and b) enhanced vertical heat fluxes due to wind driven mixing.
- Boundary current strengthening accompanied by shoaling of the Atlantic Water layer is a secondary factor leading to large melt rates.

Abstract

The ocean is suggested to play a major role in the ongoing winter decay of the sea ice cover in the western Eurasian Basin. Using a high-resolution sea ice-ocean model, we investigate the processes influencing the ice-ocean interactions in winter in the waters north of Svalbard, with a particular focus on those contributing to sea ice melt events of large amplitude. These short term events, lasting 5-10 days, are associated with locally large melt rates mostly found along the pathway of the Atlantic Water. The sum of all these events over the simulation period is found to contribute 40% of the total winter melt. Episodes of strong surface winds, occasionally associated with enhanced velocity shear at the mixed layer base can trigger enhanced entrainment of Atlantic Water through the relatively shallow upper thermocline in the Atlantic Water boundary current, leading to substantial ocean heat transfer to the sea ice. In some cases, strengthening of the boundary current also contributes to fueling the heat transfer to the ice. Another type of large melt events, not linked to increased ocean vertical heat flux but due to ice being advected over warm surface waters is also identified, sometimes associated with episodes of ice close-up. Sea ice budget calculations show that, overall, large melt events contribute significantly to the eastward retreat of the winter marginal ice zone on the upper slope east of Svalbard while episodes of northward advection of ice largely dominate the ice edge retreat over the shelf north of Svalbard.

Plain text summary.

Model simulations show that large sea-ice melt events can be found in winter within the Arctic pack ice. These events are generated by a transfer of heat from the underlying ocean to the sea ice. The melt is mainly confined above the Atlantic Water boundary current which is known to carry warm water from the Atlantic Ocean to the Artic. During periods of strong winds, part of the heat stored in the subsurface Atlantic Water reservoir can be transferred to the surface layer to help melt the ice. On some occasions, a strengthened current contributes to bringing warm water closer to the ocean surface, reinforcing the wind effect. Large melt rates are also found when ice is being moved over warm surface waters.

1. Introduction

The negative trend in the Arctic sea ice extent is characterized by a regional dependency and acceleration in the recent years (Close et al., 2015; Onarheim et al., 2018). In the Atlantic sector of the Arctic, the negative trend is larger in winter and is marked by a northeast retreat of the sea ice edge north of Svalbard (Onarheim et al., 2014). This decadal trend has been shown to be linked to oceanic influence and the Atlantic Water (AW) heat transport (e.g., Årthun et al., 2012; Ricker et al., 2021), which can lead to significant skill in decadal Arctic sea ice prediction in the Atlantic sector (Yeager et al., 2015, Årthun et al., 2017). The regions of skillful prediction could extend farther east into the Nansen Basin in the near future (Årthun et al., 2019).

The AW flows into the Arctic via the Barents Sea and Fram Strait branches. The former one loses a large part of the transported heat before entering the Arctic through St Anna Trough (Skagseth et al., 2008). The second branch is indeed the main heat source for the Arctic Ocean. The AW is carried from Fram Strait into the Arctic Ocean via different pathways which have their common source in the West Spitsbergen Current (Aaagaard et al., 1987; Cokelet et al., 2008; Crews et al., 2019; Meyer et al., 2017; Koenig et al., 2017; Menze et al., 2019) and then merge east of Svalbard to form a 30-50 km wide eastward boundary current along the southern slope of the Nansen Basin (Våge et al., 2016; Pérez-Hernández et al., 2017).

Several studies have indeed pointed out the role of the AW in the decline of the winter sea ice cover in the Eurasian Basin during the recent decades (Polyakov et al., 2010; 2017; 2020b). The growing role of the AW in this decline is attributed to AW warming and weakened stratification in the upper halocline known as the “Atlantification” of the Arctic Ocean. First detected in the Barents Sea and western Nansen Basin, as patterns of enhanced sea ice thickness decrease along the AW pathway (Ivanov et al., 2012), the impact of the ocean is now detected in the eastern Eurasian Basin where weakening of the stratification in early winter would

82 precondition the region to enhanced winter ventilation and substantial heat flux from the AW
83 layer to the sea ice (Ivanov et al., 2016; Polyakov et al., 2020b). The resulting decrease in winter
84 sea ice growth would have contributed to the recent negative trend in the winter sea ice
85 thickness in this region in similar proportions to the thermodynamic atmospheric forcing
86 (Polyakov et al., 2017). Both thermal and haline convection would play a major role in this
87 mechanism, but the increase of the velocity shear, coupled with a weakening of the stratification
88 could also potentially increase the vertical heat fluxes through enhanced vertical mixing
89 (Polyakov et al., 2020c).

90 The region north of the Svalbard archipelago is the place where the AW encounters the sea ice
91 and contributes to significant ice melt through the release of large amounts of heat to the surface.
92 On average, in the region extending immediately north and east of Svalbard (hereafter referred
93 to as the North Svalbard region) the sea ice budget is dictated by a balance between the
94 southward ice transport into the region and bottom melt fed by the convergence of warm AW
95 (e.g. Duarte et al., 2020). The AW layer is found just below the surface mixed layer, and large
96 vertical heat fluxes in the range 240-300 W/m^2 have been measured in the upper thermocline
97 on the shelf north of Svalbard in winter and, with same order of magnitude, in the under-ice
98 boundary layer (Sirevaag and Fer, 2009). These values contrast with the central Arctic Ocean
99 where weak vertical mixing at intermediate depth is responsible for small vertical heat fluxes,
100 on order of 1 W/m^2 or less at the top of the AW layer (Guthrie et al., 2013; Carmack et al.,
101 2015).

102 The winter sea ice extent in the North Svalbard region is subject to large interannual variability
103 being the result of both ocean and atmosphere variability. While, on the long-term, these
104 variations correlate significantly with the AW temperature anomalies (Onarheim et al., 2014),
105 ice advection was found to explain most anomalous winter sea ice seasons of the period 2012-
106 2019 (Lundesgaard et al., 2021). On shorter time scales, occurrences of large ice-free areas in

mid-winter are suspected to be associated with enhanced ocean influence along the AW pathway over the recent years (Ivanov et al., 2016). AW influence is effective despite the existence of a strong halocline which normally isolates the AW from the cold, fresh Polar Water filling the upper 20-30 meters of the water column as a result of annual sea ice melt (Rudels et al., 2004). Indications of deep reaching winter mixing were indeed reported for winter 2013 over the Eurasian slope at 30°E, when winter convection reached into the AW layer down to 400-500 m (Pérez-Hernández et al., 2019). In winter 2015, during the N-ICE2015 drift experiment in the waters north of Svalbard, entrainment of AW was observed to be enhanced during storm events, leading to ocean-ice heat flux of several tens of W/m^2 on average when, at the same time, the AW layer depth was particularly shallow (Meyer et al., 2017). Composite estimates of the sea ice melt rates focusing on the major storms in the same period would even lead to higher values on order of 200-300 W m^{-2} (once converted into ice-ocean heat flux), peaking at up to 600 W m^{-2} over the AW pathway (Graham et al., 2019).

The above results were obtained from a limited number of events, and for a particular winter (2015) with low sea ice conditions and would deserve a robust assessment over a longer time span using a consistent evaluation of the ice-ocean interactions. Such an approach was used recently by Duarte et al. (2020) with a one-dimensional sea ice model coupled to a slab ocean. While their model results show consistent order of magnitude between observed sea ice melt rates and the model predictions in a number of case studies, the idealized ocean model physics, especially water column restoring to observations to account for the missing physics (e.g. ocean advection), call for a more detailed representation of the ocean in order to assess the relative importance of the various processes at play. Moreover, sea ice melt rate estimates rely on sea ice budgets which are subject to large uncertainties due in particular to the low spatial resolution of the sea ice drift satellite products and the largely unknown sea ice thickness.

An interesting question is to evaluate the separate contributions of forcing and ocean preconditioning to the variability of the ocean-ice heat fluxes. In all the cases mentioned above, vertical mixing appears to be largely influenced by the three-dimensional distribution of the AW and halocline layer, in particular, the actual depth of the upper AW layer interface. The latter controls the reachability of the subsurface heat reservoir for vertical mixing. In the eastern Eurasian Basin, recent shoaling of the AW layer was indeed found to contribute to enhancing winter convection (Polyakov et al., 2020b). According to the simplified dynamic framework of an idealized slope current, the equilibrium depth of the AW layer is set by a balance between lateral mean and eddy transport and vertical diffusion, with the halocline rising toward the basin periphery, over the core of the Atlantic boundary current (Spall, 2013). However, the mechanisms underlying the variability of the halocline depth are still debated. Over the upper slope at 30°E, the upper part of the halocline was observed to rise to depths as shallow as 25 m (Pérez-Hernández et al., 2019; Renner et al., 2018). Shelf break upwelling (e.g. Lind and Ingvaldsen, 2012) may also help occasionally bring the AW layer closer to the surface, a mechanism which has been already documented by Pickart et al., (2009) off northern Alaska, and mentioned by Falk-Petersen et al. (2015) to possibly explain the presence in winter of AW in surface north of Svalbard. Similarly, Ekman pumping in response to cyclonic surface wind stress curl can lead to significant (order of 20 m over one month) shoaling of the AW layer on the northern Barents Sea slope (Renner et al., 2018). Despite these valuable observations, the variability of the AW layer geometry and how this influences the distribution of the sea ice melt in the North Svalbard region is still largely unknown.

To identify the dominant factors controlling the upward heat transfer to the under-ice ocean layer and ultimately the sea ice in the North Svalbard region, in this study we investigate the large-scale ocean conditions that could lead to enhanced influence of the AW on the winter sea ice and evaluate the contribution of the associated sea ice melt to the winter sea ice distribution.

By focusing on the intra-seasonal variability of winter sea ice melt, we aim to identify the preferred areas and the conditions of occurrence of the most significant short-term melt events and to assess their contribution to the mean winter sea ice budget. The analysis is primarily based on results of a sea ice-ocean simulation covering the period 1997-2017, therefore providing a temporal context to earlier studies based on shorter-term observations.

2. Data and model set-up

The outputs of a simulation with a regional coupled sea ice-ocean model are used to analyze the relationship between the sea ice variability and the AW properties and circulation. The model is based on NEMO (Nucleus for European Modelling of the Ocean) version 3.6 (Madec, 2008) coupled to the LIM3 (Rousset et al., 2015) sea ice model. The equations are discretized on 75 vertical levels with thickness varying from 1 m in the top layer to roughly 250 m at the deepest model level. Partial steps are used to better represent the bottom topography. A turbulent kinetic energy closure scheme that represents the evolution of the turbulent kinetic energy is used for vertical mixing of momentum and tracers (Blanke and Delecluse, 1993). The model grid has a horizontal resolution varying from ~ 2.5 km in the Arctic Ocean to 4 km in the subtropics. The domain encompasses the Arctic Ocean and the North Atlantic Ocean, with open boundaries at 28°N in the Atlantic and at Bering Strait, along which the velocity and tracer distributions are prescribed from the 5-day outputs of a global ¼° resolution hindcast simulation which has been run by the Drakkar group (https://www.drakkar-ocean.eu/) over the same period and using the DFS5 surface forcing (Dussin et al., 2018).

The model is initialized from rest with initial temperature and salinity distributions from the PHC 3.0 global ocean climatology, updated from Steele et al. (2001). The model surface forcing is based on 6-hour surface atmospheric fields from the ERA-I reanalysis (Dee et al., 2011). Turbulent heat fluxes are computed using the Large and Yeager (2004) bulk formulae with

daily dew point temperature, surface air temperature, wind speed and sea level pressure (SLP) as the main atmospheric inputs. Other forcing fields from the reanalysis include the 10-meter wind and the downward radiative fluxes. Surface albedos and temperatures simulated by the model are used to calculate the upward components of the radiative fluxes. Regional corrections have been made to improve the radiation fluxes over the North Atlantic and the surface air temperature over the Arctic. All corrections have been applied to the annual climatological cycle (obtained by averaging the daily fields between the 34 years of the reanalysis), while the field anomalies (obtained by subtracting this climatology from the original daily fields) are kept unchanged. Over the Atlantic Ocean, the ISCCP (International Satellite Cloud Climatology Project) radiation climatology (Rossow and Schiffer, 1999) is used instead of ERA-I while in the Arctic Ocean (north of Fram Strait) the ERA-I air temperature climatology is replaced by the IABP (International Arctic Buoy Programme) climatology (Rigor et al., 2000) in order to remove unrealistic positive summer values. Precipitation is extracted from the DFS5 forcing fields (Dussin et al., 2018), which are derived from ERA-I. Continental runoff is prescribed from the monthly climatology of Dai and Trenberth (2002). The simulation is performed over the period 1995-2017, and the analysis is based on the period 1997-2017. Restoring of the surface salinity to the PHC climatology is applied with a time scale of 30 days in the first 9 years but not applied for the remaining 14 years of the simulation.

To assess the simulated sea ice variability against observations we use daily sea ice concentrations (SIC), which are estimated from satellite borne passive microwave radiometer (the Special Sensor Microwave / Imager (SSM/I) and Special Sensor Microwave / Imager Sounder (SSM/IS)) observations by applying the ARTIST Sea Ice (ASI) algorithm (Kaleschke et al., 2001) and are provided on a 12.5x12.5 km grid.

The present analysis is based on 5 day-average model outputs. Winter is defined as the period extending from December to March, November and April being excluded as transition months

between seasons (the year attributed to each winter corresponds to that of January). The variability is characterized based on 5-day averaged anomalies which are constructed by removing separately for each year, the average of the winter period. The reconstructed anomalies thus characterize the intra seasonal variability over the winter period (hereafter referred to as the *winter variability*) without incorporating the interannual and longer-term variability.

3. Results

3.1 Simulated mean AW pathways and transports

Figure 1 shows the simulated mean depth of the 0°C isotherm (which can be viewed as the upper limit of the AW layer) and velocity at 60 m, in the upper part of the AW core, averaged over the period 1997-2017. North of Fram Strait, the current splits into three branches, in agreement with earlier descriptions of the circulation in this region (e.g. Aagaard et al., 1987; Koenig et al., 2017; Crews et al., 2019): the Svalbard Branch which stays south of the Yermak Plateau on the upper slope north of Svalbard, the Yermak Pass Branch which flows over the plateau and the Outer Yermak Branch which tends to follow the slope around the plateau. Northeast of Svalbard, the different branches merge into a boundary current which is localized between the 250 and 1000 m isobaths. The width of the current (30-50 km) and the seasonal evolution of the AW T S properties, with shallower, warmer core in the fall-winter season (Fig. S1 and S2) are consistent with earlier observations, as well as the spatial distribution of the properties in late summer (Fig. S3) (Våge et al., 2016; Pérez-Hernández et al., 2017). Yet, the onset of the AW warming occurs later in the model as compared with the observations, leading to overestimated AW temperature in winter. When computed with the same criteria as those used by Perez-Hernandez et al., 2019, the model AW transport averaged over the period 2012-2013 agrees well with observations over the same period (Perez-Hernandez et al., 2019) with

an annual mean of 2 Sv and a similar seasonal evolution (Fig. S4). A model-data comparison performed upstream in Fram Strait shows reasonable agreement between the model and the observations also in the West Spitsbergen Current, yet with a current velocity core slightly shifted offshore in the model (Fig. S5-S6). More details on the model skill in representing the Atlantic Water properties and transports can be found in the Supporting Information.

3.2 Winter variability of the sea ice concentration

The mean winter distributions of sea ice concentration and thickness simulated by the model are in reasonable agreement with available observations, although systematic bias toward a more compact, thinner ice cover can be identified in our region of interest (see supporting information, Fig. S7 for further details). To determine the spatial and temporal structure of the *winter variability* of the ice cover, an empirical orthogonal function (EOF) analysis has been performed on the SIC observations over the period 1997-2017 and the domain 79°N-84°N, 0°E-50°E (Fig. 2). The EOF analysis shows occurrences of short-term (duration of 5-20 days) low sea ice concentration events extending all along the northern Svalbard and Barents Sea slope area (Fig. 2b), including large amplitude events in winter 2000, 2006, 2013 and 2017 (Fig. 2c).

A similar analysis has been performed on the simulated SIC over the same period (Fig. 2a,c). Similar major low concentration events are found in the simulation, and the correlation between the first principal component of the observed and simulated SIC is 0.74, suggesting that the model reproduces rather well the *winter variability* of the SIC (Fig. 2c). However, the loading pattern of the simulated SIC does not extend as far northward and eastward. The origin of the discrepancy is a persistent overestimation of the winter sea ice extent in this region in the simulation, with the marginal ice zone (MIZ, defined as the region where the sea ice concentration is between 15 and 80% and is expected to be the most variable), being located more persistently over the shelf than over the slope region like in the observations. The first

EOF of the simulated sea ice thickness (not shown) displays a similar loading pattern as the SIC, and the correlation of 0.75 between the respective principal components suggests similar time evolution for the two properties.

3.3 Contribution of the melt to the sea ice volume budget.

As shown in Figure 3a, which displays the mean winter sea ice volume change over our study area (see the geographical extent of the study area in Fig, 2a), sea ice on average tends to grow throughout the winter season over the entire area (here and in the following the ice volume stands for ice volume per unit area). While no particular pattern of this winter growth is found over the upper slope area (the region encompassed between the 250 m and 1000 m isobaths), both its dynamic (transport convergence) and thermodynamic contributions show a pattern of large convergence and melt aligning with these isobaths (Fig. 3c,e). Enhanced convergence there coincides with weaker thermodynamic growth or even net melt, which extends eastward into the inner pack (the pattern is almost identical if one selects only melt occurring in locations where the SIC is larger than 80%). The signature of enhanced melt, concentrated over the AW current path (compare Fig. 1 with Fig. 3e), is consistent with a response to higher ocean heat flux in this area (Fig. 3b). The mean winter melt is in part due to short term (5-10 days) large melt events (Fig. 2d, see next section for an explanation of the index), which can lead to major ice volume decrease as observed, for instance, in January or in February 2006 (Fig 4a, green line). The standard deviation of the thermodynamic contribution (Fig. 3f) to the mean winter ice volume change averaged over the study area remains, however, 3 times smaller than that of the dynamic contribution (Fig. 3d) over the full period of the simulation. Actually, large ice volume changes driven by variations of the ice transport convergence (Fig. 3d), although affecting primarily the MIZ over the shelf north of Svalbard, also extend into the pack ice interior, immediately east of Svalbard. By contrast, the thermodynamic contribution affects the ice volume over the AW current pathway (Fig. 3f).

3.4 Large melt events.

To characterize the episodes of large melt and identify their likely causes, a time series of the area-weighted ice melt rate has been built by averaging only negative values of the net growth rate (or equivalently setting growth rate to zero where positive) over the study area. Doing so we aim to better represent the episodes of large melt, without incorporating the compensating effects of areas of positive net growth (note that changes in the melt rate amplitude were found to dominate over changes in the area of melt in the index variability). We then define a melt index by removing, separately for each year, the mean of the winter period to construct winter melt anomalies (Fig. 2d). Large melt events have been defined as those for which the index is larger than 1 standard deviation (similarly occurrences of low melt are defined as those for which the index is smaller than 1 standard deviation). Over the 1998-2017 winter period 46 5-day episodes of large melt are found, of which 12 contribute to pairs of consecutive episodes, leading to a total of 40 large melt events with duration ranging between 5 and 10 days. The amplitude and number of large melt events per winter are quite variable (the number ranges from a maximum of 5 events in 2001 to none in 2014) but, in total, they account for about 40% of the cumulated winter melt over the whole period. In the next section, we analyze three large melt events which occurred in 2006 and were associated with different driving processes. Then, we will evaluate the relevance of the conclusions drawn from these events to the other large melt events.

3.4.1 Case study: large melt events in 2006.

During winter 2006, the ice cover starts to decrease on January 10 in response to large divergence of the ice volume transport (Fig. 4a). The decrease accelerates on January 15, due in particular to a large melt event, before the SIC reaches a minimum on January 25. From January 30 the ice cover starts to reconstruct due to ice being transported into the study area,

but the ice close-up is slowed down due to a second large melt event between February 24 and March 1 which tends to oppose a concomitant large convergence event.

During the first large melt event, the melt increases concomitantly to the occurrence of strong southeasterly wind (Fig. 4b and 5a), and melt rates larger than 6 cm/d can be observed within the pack ice over the path of the boundary current (and also in the Kvitoya Trough) (Fig. 5b). The melt pattern coincides with large values of ice-ocean heat flux which can reach more than 400 W/m^2 (Fig. 5c). A vertical section across the shelf-slope area at 31°E shows that the largest melt rates are found just above the region where the AW layer is closer to the surface (the depth of the 0°C isotherm is about 15-20 m) and the largest vertical diffusive heat flux and the warmest temperature can be observed (Fig. 6a,b). The vertical diffusive flux is responsible for the heat transfer from the upper part of the pycnocline to the surface layer. Between 81°N and 81.4°N, the maximum of this flux is in the subsurface and the flux decreases towards the surface in the upper 10 meters suggesting a convergence of heat and a warming of this layer. Between 81.45°N and 81.6°N the vertical gradient of the diffusive heat flux is of opposite sign, suggesting an additional heat source near the surface. However, when forming a heat budget for the upper 10 meters of the water column over the area where the melt rate is larger than 2 cm/day during the large melt event (hereafter referred to as the *melt area*), the vertical diffusive heat flux appears as the major heat source for this layer on January 15 (Fig. S8), and all this heat is lost to the ocean surface with very minor contributions from both vertical and horizontal advection. On average over the *melt area*, horizontal advection is indeed negligible, which suggests that this process mainly contributes to horizontal redistribution of the heat within the area (being responsible, for instance, for local input to the surface layer as identified on the northern part of the 31°E section). When the heat budget is computed over a layer which extends further down, below the pycnocline (Fig. S8), the dominant heat source on January 15 is provided by vertical advection, suggesting that the heat provided to the surface by vertical

328 diffusion through the upper pycnocline is refueled by vertical advection. This is consistent with
329 the positive vertical velocity found in the pycnocline (Fig. 6d). Actually, the time evolution of
330 the vertical advection contribution between January 5 and 25 follows that of the Ekman suction
331 velocity averaged over the *melt area* (later on, other processes are involved in the subsequent
332 ice opening), suggesting a response to the surface stress curl.

333 The maximum of the vertical diffusive heat flux (Fig. 6b) is found in the area of substantial
334 deepening of the mixed layer and where the mixed layer was the shallowest before the
335 occurrence of the large melt event (Fig. 6a). Here, the mixed layer is defined as the depth at
336 which the potential density exceeds the surface density by 0.1 kg/m^{-3}. The maximum of the
337 diffusive heat flux also coincides with a narrow area where both the strongest near-surface
338 stratification (maximum of the Brunt Väsäilä frequency) (Fig. 6f), and the maximum vertical
339 shear of velocity (Fig. 6e) are found. A vertical profile in the area of large heat flux (Fig. S9)
340 shows that the Richardson number (computed using 5-day averaged variables) remains close to
341 the critical values at the base of the mixed layer, suggesting that enhanced mixing is not only
342 due to an increased input of energy at the surface by larger surface stress but might also result
343 from increased shear instability at the mixed layer base. The January large melt event
344 contributes to eastward expansion of the ice pack opening (compare SIC isopleths on January
345 15 and 20 in figure 5b) that has started on January 10 (Fig. 4a).

346 Between February 24 and March 1 2006, a second large melt event occurs (Fig 4a) but the
347 driving processes are distinct from those explaining the first event. On February 24, the MIZ
348 north of Svalbard is fairly far north (Fig. 7c), as a consequence of the large ice opening which
349 started at the beginning of January, and open water occupies a large area north of Svalbard,
350 extending from the shelf northeastward to the slope region. Then, the large persistent northerly-
351 northwesterly winds (Fig. 7a) during the next days drive a westward-southwestward ice drift,
352 advecting the ice pack over the warm water present on the shelf-upper slope (Fig. 7g). The large

353 melt rate area (Fig. 7c) coincides indeed with the area of large ice transport convergence (Fig.
354 7e). Despite it being a large melt event, this event is thus associated with a close-up of the ice
355 pack (Fig 4a).

356 During the next winter, on December 26, 2006, a third large melt event begins, which is less
357 intense than the two previous ones (Fig. 4a and 8g). The event, which is marked by moderate
358 wind anomalies (Fig. 4b, 8a), lags by 1-2 weeks a strengthening of the boundary current
359 between December 1 and December 16 (Fig. 4b and 8c). The increase of the current which can
360 be traced back into the WSC, is associated with shoaling of the AW layer along the AW
361 pathway in our study area (Fig. 8e and 9a,b). Despite moderate winds, these oceanic conditions
362 may have favored enhanced vertical mixing on December 26, with a deepening and warming
363 of the mixed layer, and subsequent ice melt (Fig. 9c).

364 3.4.2 Large melt events over the simulation period

365 Building on the information gained from the 2006 case study, we pursue the analysis by
366 performing a more systematic analysis of the large melt events over the full period of the
367 simulation. Composites are constructed based on indices which best represent the different
368 mechanisms that have been identified in the previous section in relation to the large melt events
369 of year 2006.

370 3.4.2.1 Large melt associated with ice advection over warm water.

371 In order to identify the large melt events which are associated with advection of ice over warm
372 water, we define a sea surface temperature (SST) index as the average of the SST over the *melt*
373 *area*. After analyzing the time evolution of the sea ice response, a time lag of 5 days was
374 identified as the lag of maximum response and, therefore, the SST index is based on the SST
375 averaged over the 5 days preceding the melt event. Composites of the ice melt rate averaged
376 over the large melt events which are associated with a value of the SST index higher than -

1.5°C are constructed. 8 such large melt events are identified (Fig. 10), with two of them lasting 10 days. The melt pattern associated with these events indicates enhanced melt occurring predominantly to the west of 27°E and mainly in the MIZ (Fig. 7d). As described for the second large melt event of the winter 2006, these large melt events are associated with high ice volume transport convergence (Fig. 7f), a process which is likely driven by strong northeasterly winds, as shown by the corresponding composites of the surface wind (Fig. 7b). In that case the convergence of the transport is due to advection of ice over open water, which is consistent with an ice edge being advected over the warm water pool located to the southwest of the ice edge (Fig 7h). The ice transport tends to overcompensate the ice melt, a balance which leads to an expansion of the ice cover (compare the black and blue lines in Fig. 7h). These close-up episodes can be consecutive to ice opening events (Fig. 10), which, as in 2006, can be sustained more than one month.

3.4.2.2 Melt driven by large surface stress events

During the January 2006 event, wind driven mixing is the dominant mechanism. We then investigate if this process can drive other large melt events. Accordingly, we define a surface stress index by averaging, over the study area, the magnitude of the stress at the ocean surface (defined, for a given model grid cell, as a combination of the ice-ocean stress in the ice-covered part of the grid cell and the wind stress over the ice-free part). Large stress events have been defined as those which are associated with stress anomalies of amplitude larger than 1 standard deviation. 25 out of the 36 5-day periods of large melt which are not preceded by warm SSTs are associated with large stress (Fig. 10). The composite of the melt rate averaged over these events (Fig.11a) differs from the pattern in Figure 7d and displays a pattern with an enhanced signature above the boundary current pathway which extends eastwards into the pack ice as far as 40°E (a similar pattern is obtained when the composite is calculated over areas where the SIC exceeds 80%).

The pattern of the melt reflects that of the mean depth of the 0°C isotherm, with areas of larger melt located over shallow 0°C isotherm (compare Fig. 11a with Fig. 1). The largest melt is found around 24°E, where the boundary current narrows and the 0°C shoals due to the steep topography. A vertical section along 24°E shows the deepening of the mixed layer during the large melt events accompanied by the formation of negative temperature anomaly in the pycnocline just below the area of large melt (Fig. 11b). This would be consistent with an enhanced vertical heat flux from the pycnocline to the ocean surface, with a part being lost to slightly warm the mixed layer. North of the boundary current, where the mixed layer is deeper and the vertical temperature gradient is weaker, vertical mixing is not strong enough to affect significantly the ice melt. More generally, while the mean depth of the upper boundary of the AW layer is decisive for the pattern of sea ice melt, the composite differences of the AW depth based on the large melt events associated with large stress do not show significant anomalies, suggesting that Ekman suction anomalies would only contribute to sea ice melt in some specific cases as in January 2006.

These large melt events are not linked with a preferred wind direction (Fig. S10). This finding is consistent with correlation maps (not shown) between the melt index and the zonal and meridional components of the 10 m wind which do not display absolute values exceeding 0.2. In contrast, the correlation map of the melt index with the wind speed indicate absolute values of 0.4-0.5 north of Svalbard.

While wind driven mixing appears to be the dominant process to generate large melt events, not all the large melt events are associated with strong winds, and only slightly more than 50% of the large stress events can be linked to large melt events suggesting that other processes might modulate the melt.

3.4.2.3 Influence of the boundary current.

As aforementioned, the pathway of the boundary current is reflected in the pattern of the ice melt, suggesting that the current may play a role in the *winter variability* of the ice melt. A velocity index is thus defined based on the along-slope velocity distribution at 20°E, downstream of the merging of the AW Svalbard and Yermak branches. The index represents the mean velocity over the upper part (between 20 and 40 m depth) of the current core and does not consider the velocity variations in the Ekman layer. The composite of the mean velocity anomalies in the layer 20-40 m averaged over the strong current events (i.e events for which the velocity index exceeds 1 standard deviation) suggests a strengthening of the boundary current which occurs all along the current pathway, including in its upstream region in the WSC (see Fig. 8d). This anomalous circulation appears to be associated with anticyclonic wind anomalies centered on the northern Barents Sea (Fig. 8b). These strong current events are more persistent than the large melt events: their mean duration is about 15 days, but they can last up to 25 days. They are linked with a shoaling of the 0°C isotherm (Fig. 8f), and subsurface warming along the AW pathway, with the strongest values located east of 24°E (not shown). This warming remains significant when the temperature lags by 10 to 15 days. It is also interesting to notice the local impact of these strong current events on the surface stress, which depends, in ice covered areas, on the relative velocity of the ice with respect to the ocean surface current. During these events, a dipole pattern of the surface stress curl is observed along the path of the boundary current (Fig. 12), which could contribute to the shoaling of the AW layer.

Based on the boundary current velocity index, we identify 17 5-day episodes of large melt events which are preceded by or in phase with strong current events (Fig. 10a). With the increase of the subsurface heat content, the strong current events generate favorable ocean conditions for increased vertical transfer of heat through mixing to the ice (Fig. 8h). This mechanism does not require strong winds, as demonstrated by the significant proportion (6 out

of 17) of events which occur during moderate surface stress conditions, and by the event documented on December 25, 2006.

4. Discussion

Focusing on the *winter variability* of the coupled ice-ocean system north of Svalbard, we have shown that sea ice melt can occur as large amplitude, short term (5-10 days) events, which are mainly located over the AW pathway. Large melt rates are found in the MIZ but also in the interior pack ice where they can reach as far east as 40°E. Concomitant direct observations of sea ice melt rates and ice-ocean heat fluxes are too sparse to enable systematic validation of the model results. However, local observations of large ice-ocean heat fluxes during the N-ICE2015 drift (Meyer et al., 2017; Graham et al., 2019), can be used to check if these are concomitant to simulated large melt events. The first of these large flux events which occured during a storm between February 3 and 9 indeed emerges as a large melt event in our simulation, being identified as an event of advection of ice over warm waters (Fig. 10). An episode of strong northerly winds between February 6 and 9 (also mentioned by Graham et al., 2019), indeed followed strong southerly winds during February 4 to 5 which might have led to an ice cover opening. The second observed event also occurred during a storm and the model does show an increase of the 5-day averaged melt rate over the period including this storm (not shown), but not high enough for this event to be identified as large melt event. The reason for the low melt rate may be related to the spatial-temporal distribution of the wind anomalies. The strong winds were mostly confined to the northwestern part of our study region (not shown) and lasted only one day, and therefore might have not appeared as strong enough when averaged over the study area and a 5-day period.

An increase of the ice-ocean heat flux was indeed observed to coincide with storm activity and the presence of AW in the sub-surface ocean in earlier observations (Meyer et al. 2017; Graham

et al., 2019). In our simulation wind driven mixing, entraining warm AW into the upper layer, appears as the dominant mechanism generating large ice melt events. These episodes of enhanced mixing correspond to above-average ocean surface stress. Although 5-day averaged wind events are used in this analysis, the role of high frequency atmospheric forcing is certainly important. For instance, the largest melt event on March 11, 2004 (Fig 10a), is linked to a moderate 5-day average surface stress (Fig. 10b), while wind data at higher temporal resolution indeed reveal weak winds over this 5-day period except for a short (1 day) wind burst. To investigate if some of the melt events may be mis-classified with regards to the strength of the wind stress forcing, we compare two wind speed indices. One is based on the maximum of the 5-day averaged wind speed (the surface stress, which is an output of the model saved every 5-day and cannot be used here) and the other is based on the 5-day mean wind speed. Both indices are averaged over the study area. The two groups of large melt events associated with large values (i.e > 1 std) of these two wind indices are very similar, suggesting the robustness of our analysis based on 5-day averages.

Only 55% of the large stress events present in the simulation are associated with large melt events, 45% of the large stress events are thus associated with moderate melt events. Part of the explanation may be found in the different surface stress distributions between the two groups of melt events which reveal a comparatively lower mean stress and absence of very large stress events in the moderate melt group. However, even when restricting the comparison between the two groups to events with stress lower than 0.13 $N.m^{-2}$ (so that the mean stress of the two groups become similar) we find that the vertical shear of the current at the base of the mixed layer in the *melt area* is indeed drastically reduced during moderate melt events compared with the large melt events (the difference between the mean shear of the two groups is large and statistically significant). This increased shear is also accompanied by a significant strengthening of the stratification during the large melt events, but overall, the area where the Richardson

number remains in the range of the critical values is significantly larger in the large melt group, suggesting that shear instability could contribute to enhance the vertical heat fluxes and the melt rate during large melt events.

The mean melt rate in our simulation is clearly shaped by the depth of the upper boundary of the AW layer (taking, e.g., the depth of the 0°C isotherm as a proxy for the upper limit of this layer), with the largest melt located above regions where the AW layer is shallower. This is a strong suggestion that the topography of the AW layer maintained by the boundary current exerts some preconditioning with regards to further vertical mixing events. However, melt events triggered by large surface stress (which represent the large majority of the large melt events) are not sensitive to the depth of the AW layer. While this may be partly due to the weak variability of the AW layer, it also suggests that upwelling (in particular shelf break upwelling in the region of enhanced melt) cannot be a leading mechanism in producing large sea ice melt, a result which is probably linked to the rather deep shelf found north of Svalbard (as already mentioned by Randelhoff and Sundfjord, 2018). Some occurrences of AW upwelling can however be identified which lead to subsurface warming and enhanced upward heat fluxes and sea ice melt. In such cases, the AW layer rise would accompany a strengthening of the boundary current which may have been forced by an anticyclonic wind anomaly centered over the northern Barents Sea. This latter finding is consistent with conclusions by Lien et al. (2013) and Herbaut et al. (2017) who suggested that negative wind curl over the Northern Barents Sea could enhance the anticyclonic circulation on the shelf around the Svalbard Archipelago, and in particular strengthen the boundary current in the western Eurasian basin. However, the impact of the current on its own may be limited since, despite 50% of those large melt events not associated with ice advection over warm SST appear to be preconditioned by large current, most of these large current events need large stress to trigger a large response of the sea ice melt.

None of the large melt events show significant deepening of the surface mixed layer in the simulation. In addition, buoyancy driven convection does not seem to play a role in the occurrence of large melt events since only one episode of deep convection is detected in our study area. The event occurs in the boundary current during periods of ice-free conditions and can lead to mixed layers as deep as 300-400 meters. Buoyancy driven convection has been mentioned as the process responsible for winter ventilation of the Atlantic Water layer in the interior ice pack in the deep Nansen Basin (Polyakov et al., 2017, 2020). Occurrences of ocean convection under low sea ice concentrations, as found in our analysis, have also been reported in the literature in observations (Pérez-Hernández et al., 2019) and ocean model operational systems (Athanase et al., 2020). While convective mixing in open water does not contribute directly to sea ice melt in our simulation, it does contribute in a delayed mode to the sea ice volume budget by transferring large amounts of heat to the surface layer and thus slowing down the return to heavier ice conditions. Advection of ice into surface waters which have been previously warmed by convective mixing can indeed generate large melt events subsequently to the convective events.

The January 2006 case study illustrates how large melt rates can contribute to the eastward retreat of the ice edge north of Svalbard in mid-winter. Composites of the SIC change during large melt events over the entire simulation show that the largest reduction in the sea ice concentration is usually found over the shelf north of Svalbard, decreasing to values less than 10% over a 5-day period further offshore, while northeast of Svalbard, as far as 36°E, anomalies do not exceed 5% (Fig. 13a). However, similar composites based on the events of large ice transport divergence do not show the same decrease of ice concentrations northeast of Svalbard (Fig. 13b) which suggests that ocean-driven sea ice melt is the main mechanism responsible for the episodes of sea ice concentration decrease observed northeast of Svalbard. Conversely, on the shelf north of Svalbard, the SIC decrease is mainly explained by large divergence of the ice

549 volume transport, which is driven by southeasterly wind (not shown) enhancing northward
550 advection of thinner ice from the south (Fig. 13c).

551 This mechanism was also mentioned by Onarheim et al., (2014) to explain the interannual sea
552 ice variability in the same region. However, while these authors only stressed the impact of the
553 wind stress on the ice transport, we could show that, in case of particularly high wind speed, a
554 thermodynamic effect can add to the dynamic response of the ice. Because of this additional
555 effect, the impact of the wind on the sea ice may be stronger than previously postulated. In
556 particular, during periods of large southerly winds, larger ice divergence and enhanced
557 entrainment could combine to drive particularly large ice cover decrease, with each process
558 driving ice reduction over a specific distinct area. Actually, the four largest ice cover decrease
559 events in 2000, 2006, 2013 and 2017, as identified by the EOF analysis of the winter SIC (Fig.
560 2), occurred during periods of large southerly winds (not shown).

561 Graham et al., (2019), using ice drift and area from satellite observations and constant ice
562 thickness to compute the ice volume budget, estimate that over a domain equivalent to our study
563 area, ice-ocean heat flux up to 600 W/m^2 (to account for the melt rate estimated) over about 2
564 days could occur during a storm. In the simulation such large ice-ocean heat fluxes can happen
565 in localized areas but on average over the study area, the 5-day heat fluxes exceed only twice
566 100 W/m^2 (Fig 2e). This discrepancy between the heat fluxes can be due to the model limitations
567 and to the large uncertainties inherent of the method used by Graham et al. (2019).

568 Over the time of the simulation, we do not find significant correlation between a preferred wind
569 direction and sea ice melt index. This finding is in contrast to Duarte et al.'s (2020) conclusion
570 which highlights significant correlations between southeasterly winds and sea ice melt rates.
571 The fact that Duarte et al. calculation is done over a region that is located closer to the ice edge
572 and further west compared to our study area may explain the discrepancy. This limitation in the

573 comparison is even reinforced by the fact that, as aforementioned, the processes highlighted in
574 our simulation take place in an area which is mainly covered by compact ice. In contrast, the
575 domain analyzed by Duarte et al. includes a larger fraction of the MIZ where, under northerly
576 winds, ice advection can lead to large melt when ice encounters warm waters.

577 The goal of the present analysis was to explore the sensitivity of the Arctic sea ice cover to
578 some ocean processes. As such, it emphasizes the role of the mechanical surface forcing in
579 controlling important processes like vertical mixing, advection or sea ice motion, but also the
580 upper ocean temperature distribution and stratification. The sensitivity of these processes to the
581 forcing is however likely to depend on the mean sea ice state. Underestimated sea ice thickness
582 in the simulation, for instance, should imply a more efficient energy transfer between the
583 atmosphere and the ocean, an effect however modulated by the higher compactness of the ice
584 cover so that the net impact is difficult to estimate. On the other hand, due to too compact sea
585 ice in the model climatology, the SIC variability is underestimated along the AW boundary
586 current (Fig. 2) and the ice conditions simulated in this region may therefore be more
587 representative of more compact ice conditions observed farther downstream. One of the
588 consequences of this could be an underestimation of the number of large melt events associated
589 with ice advection over warm SST: with a MIZ, which would be located closer to the boundary
590 current, close-up of the ice following opening should be accompanied by larger ice-ocean heat
591 flux. While the simulated winter AW temperature distribution in the West Spitsbergen Current
592 matches reasonably well the observations in Fram Strait, the AW core appears too warm in
593 winter northeast of Svalbard. While this discrepancy might be a consequence of a shift in the
594 seasonal cycle as discussed earlier, the overestimated ice extent and compactness during most
595 of the year may also contribute to limiting direct heat loss through air sea interactions. In
596 principle, the warm bias in the upper part of the AW layer (that part which is eroded during
597 large melt events) should lead to overestimated upward heat flux and ice bottom melt under

598 vertical mixing. However, larger sea ice extent in the model is also associated with a fresher
599 ocean surface layer and a stronger upper halocline which limits the mixing efficiency and
600 mitigates the impact of warmer subsurface water, therefore suggesting that our results are
601 conservative regarding the impact of vertical mixing on the sea ice. Still, further investigation
602 would be necessary to disentangle the different contributions to the model sensitivity with
603 respect to mixing. More generally, additional observations are needed to validate the
604 relationship between winter sea ice melt and the underlying ocean dynamics and its dependency
605 on the different sea ice regimes, a prerequisite to assessing their impact on the sea ice cover at
606 the basin scale.

607 **5. Summary and conclusions**

608 Using an ice-ocean simulation forced by the ERA-I reanalysis over the period 1997-2017, large
609 ice melt events have been identified in winter in the area north of Svalbard. These short duration
610 (5-10 days) melt events, which show enhanced signature along the AW pathway and can occur
611 in the pack ice, can contribute to 40% of the total winter ice melt. The net growth pattern
612 associated with the large melt events clearly reflects the mean pattern of the 0°C isotherm.
613 Different types of events have been established depending on the scenario responsible for
614 enhanced sea ice melt. Enhanced melt can happen concomitantly to large ice transport over
615 warm surface waters in the ice edge region, a scenario which predominates during the close-up
616 following a large sea ice cover opening. This process is also a factor controlling the SIC budget
617 on interannual time scales (Lundesgaard et al., 2021) and may become more frequent in the
618 area in the future with the expansion of the ice-free areas and the ice becoming more mobile.

619 Apart from these events, large melt rates are mainly driven by increased mixing and entrainment
620 of warm water into the mixed layer. Strong winds are the main driver of the large mixing events
621 but the shoaling of the pycnocline during episodes of strengthened boundary current can also

622 modulate the vertical heat flux into the mixed layer. Shear instability is likely to enhance the
623 heat transfer to the surface layer. While wind driven mixing appears to be the controlling factor
624 of the winter sea ice melt in the western Eurasian Basin, thermohaline convection has been
625 pointed out as the main driver of the winter ice melt in the eastern Eurasian Basin (Polyakov et
626 al., 2017). With the expansion of the ocean conditions prevailing north of Svalbard to the
627 eastern Eurasian Basin as a result of the Atlantification of the Arctic Ocean (Polyakov, 2017;
628 Polyakov et al., 2020a), the nature of the drivers of the ice melt in this part of the basin may
629 also change and the impact of wind driven mixing and boundary current dynamics on the future
630 of the Arctic sea ice cover become visible on a wider scale.

631 Acknowledgement: This study was supported by the Blue-Action project, which has received
632 funding from the European Union's Horizon 2020 Research and Innovation Programme under
633 Grant Agreement No 727852. It was also supported by the French national programme LEFE
634 of the Institut National des Sciences de l'Univers, CNRS. The model code is available on
635 zenodo (https://zenodo.org/record/6546445#.YoVHJlTP02w). This work was granted access
636 to the HPC resources of CINES under allocation 20100239 made by GENCI. We thank two
637 anonymous reviewers for their very useful comments which helped improve the manuscript.
638 The model initialization is based on the PHC3 climatology
639 (http://psc.apl.washington.edu/nonwp_projects/PHC/Climatology.html). Continental runoff is
640 extracted from the monthly climatology of Dai and Trenberth (2002)
641 (https://rda.ucar.edu/datasets/ds551.0/). The atmospheric forcing is based on the ERA-Interim
642 reanalysis (https://www.ecmwf.int/en/forecasts/datasets/reanalysis-datasets/era-interim). The
643 ISCPP climatology of the radiation fluxes over the North Atlantic
644 (https://isccp.giss.nasa.gov/projects/flux.html) and the surface air temperature from the IABP
645 climatology (http://research.jisao.washington.edu/data_sets/iabppoles/) have been used.
646 Precipitation is extracted from the DFS5 dataset (https://ige-meom-opendap.univ-grenoble-

alpes.fr/thredds/catalog/meomopendap/extract/FORCING_ATMOSPHERIQUE/DFS5.2/ALL/catalog.html). The sea ice concentration data were retrieved from the Integrated Climate Data Center of Hamburg University (https://www.cen.uni-hamburg.de/en/icdc/data/cryosphere/seaiceconcentration-asi-ssmi.html).

References:

Årthun, M., Eldevik, T., Smedsrud, L.H., 2019. The Role of Atlantic Heat Transport in Future Arctic Winter Sea Ice Loss. J. Clim. 32, 3327–3341. https://doi.org/10.1175/JCLI-D-18-0750.1

Årthun, M., Eldevik, T., Smedsrud, L.H., Skagseth, Ø., Ingvaldsen, R.B., 2012. Quantifying the Influence of Atlantic Heat on Barents Sea Ice Variability and Retreat. J. Clim. 25, 4736–4743. https://doi.org/10.1175/JCLI-D-11-00466.1

Årthun, M., Eldevik, T., Viste, E., Drange, H., Furevik, T., Johnson, H.L., Keenlyside, N.S., 2017. Skillful prediction of northern climate provided by the ocean. Nat. Commun. 8, 15875. https://doi.org/10.1038/ncomms15875

Athanase, M., Provost, C., Pérez-Hernández, M.D., Sennéchael, N., Bertosio, C., Artana, C., Garric, G., Lellouche, J.-M., 2020. Atlantic Water Modification North of Svalbard in the Mercator Physical System From 2007 to 2020. J. Geophys. Res. Oceans 125, e2020JC016463. https://doi.org/10.1029/2020JC016463

Beszczynska-Möller, A., Fahrbach, E., Schauer, U., Hansen, E., 2012. Variability in Atlantic water temperature and transport at the entrance to the Arctic Ocean, 1997–2010. ICES J. Mar. Sci. 69, 852–863. https://doi.org/10.1093/icesjms/fss056

Blanke, B., Delecluse, P., 1993. Variability of the Tropical Atlantic Ocean Simulated by a General Circulation Model with Two Different Mixed-Layer Physics. J. Phys. Oceanogr. 23, 1363–1388. https://doi.org/10.1175/1520-0485(1993)023<1363:VOTTAO>2.0.CO;2

Carmack, E., Polyakov, I., Padman, L., Fer, I., Hunke, E., Hutchings, J., Jackson, J., Kelley, D., Kwok, R., Layton, C., Melling, H., Perovich, D., Persson, O., Ruddick, B., Timmermans, M.-L., Toole, J., Ross, T., Vavrus, S., Winsor, P., 2015. Toward Quantifying the Increasing Role of Oceanic Heat in Sea Ice Loss in the New Arctic. Bull. Am. Meteorol. Soc. 96, 2079–2105. https://doi.org/10.1175/BAMS-D-13-00177.1

Close, S., Houssais, M.-N., Herbaut, C., 2015. Regional dependence in the timing of onset of rapid decline in Arctic sea ice concentration. J. Geophys. Res. Oceans 120, 8077–8098. https://doi.org/10.1002/2015JC011187

Cokelet, E.D., Tervalon, N., Bellingham, J.G., 2008. Hydrography of the West Spitsbergen Current, Svalbard Branch: Autumn 2001. J. Geophys. Res. Oceans 113. https://doi.org/10.1029/2007JC004150

Crews, L., Sundfjord, A., Hattermann, T., 2019. How the Yermak Pass Branch Regulates Atlantic Water Inflow to the Arctic Ocean. J. Geophys. Res. Oceans 124, 267–280. https://doi.org/10.1029/2018JC014476

Dai, A., Trenberth, K.E., 2002. Estimates of Freshwater Discharge from Continents: Latitudinal and Seasonal Variations. J. Hydrometeorol. 3, 660–687. https://doi.org/10.1175/1525-7541(2002)003<0660:EOFDFC>2.0.CO;2

Dee, D.P., Uppala, S.M., Simmons, A.J., Berrisford, P., Poli, P., Kobayashi, S., Andrae, U., Balmaseda, M.A., Balsamo, G., Bauer, P., Bechtold, P., Beljaars, A.C.M., Berg, L. van de, Bidlot, J., Bormann, N., Delsol, C., Dragani, R., Fuentes, M., Geer, A.J., Haimberger, L., Healy, S.B., Hersbach, H., Hólm, E.V., Isaksen, L., Kållberg, P., Köhler, M., Matricardi, M., McNally, A.P., Monge-Sanz, B.M., Morcrette, J.-J., Park, B.-K., Peubey, C., Rosnay, P. de, Tavolato, C., Thépaut, J.-N., Vitart, F., 2011. The ERA-Interim reanalysis: configuration and performance of the data assimilation system. Q. J. R. Meteorol. Soc. 137, 553–597. https://doi.org/10.1002/qj.828

Duarte, P., Sundfjord, A., Meyer, A., Hudson, S.R., Spreen, G., Smedsrud, L.H., 2020. Warm Atlantic Water Explains Observed Sea Ice Melt Rates North of Svalbard. J. Geophys. Res. Oceans 125, e2019JC015662. https://doi.org/10.1029/2019JC015662

Dussin, R., Barnier, B., Brodeau, L., Molines, J.-M., 2018. The making of the Drakkar Forcing set DFS5. https://doi.org/10.5281/zenodo.1209243

Falk-Petersen, S., Pavlov, V., Berge, J., Cottier, F., Kovacs, K.M., Lydersen, C., 2015. At the rainbow's end: high productivity fueled by winter upwelling along an Arctic shelf. Polar Biol. 38, 5–11. https://doi.org/10.1007/s00300-014-1482-1

Graham, R.M., Itkin, P., Meyer, A., Sundfjord, A., Spreen, G., Smedsrud, L.H., Liston, G.E., Cheng, B., Cohen, L., Divine, D., Fer, I., Fransson, A., Gerland, S., Haapala, J., Hudson, S.R., Johansson, A.M., King, J., Merkouriadi, I., Peterson, A.K., Provost, C., Randelhoff, A., Rinke, A., Rösel, A., Sennéchael, N., Walden, V.P., Duarte, P., Assmy, P., Steen, H., Granskog, M.A., 2019. Winter storms accelerate the demise of sea ice in the Atlantic sector of the Arctic Ocean. Sci. Rep. 9, 1–16. https://doi.org/10.1038/s41598-019-45574-5

Guthrie, J.D., Morison, J.H., Fer, I., 2013. Revisiting internal waves and mixing in the Arctic Ocean. J. Geophys. Res. Oceans 118, 3966–3977. https://doi.org/10.1002/jgrc.20294

Ivanov, V., Alexeev, V., Koldunov, N.V., Repina, I., Sandø, A.B., Smedsrud, L.H., Smirnov, A., 2015. Arctic Ocean Heat Impact on Regional Ice Decay: A Suggested Positive Feedback. J. Phys. Oceanogr. 46, 1437–1456. https://doi.org/10.1175/JPO-D-15-0144.1

Ivanov, V.V., Alexeev, V.A., Repina, I., Koldunov, N.V., Smirnov, A., 2012. Tracing Atlantic Water Signature in the Arctic Sea Ice Cover East of Svalbard [WWW Document]. Adv. Meteorol. https://doi.org/10.1155/2012/201818

Kaleschke, L., Lüpkes, C., Vihma, T., Haarpaintner, J., Bochert, A., Hartmann, J., Heygster, G., 2001. SSM/I Sea Ice Remote Sensing for Mesoscale Ocean-Atmosphere Interaction Analysis. Can. J. Remote Sens. 27, 526–537. https://doi.org/10.1080/07038992.2001.10854892

Koenig, Z., Provost, C., Sennéchael, N., Garric, G., Gascard, J.-C., 2017. The Yermak Pass Branch: A Major Pathway for the Atlantic Water North of Svalbard? J. Geophys. Res. Oceans 122, 9332–9349. https://doi.org/10.1002/2017JC013271

Koenig, Z., Provost, C., Villacieros-Robineau, N., Sennéchael, N., Meyer, A., 2016. Winter ocean-ice interactions under thin sea ice observed by IAOOS platforms during N-ICE2015: Salty surface mixed layer and active basal melt. J. Geophys. Res. Oceans 121, 7898–7916. https://doi.org/10.1002/2016JC012195

Large, W.G., Yeager, S.G., n.d. Diurnal to Decadal Global Forcing For Ocean and Sea-Ice Models: The Data Sets and Flux Climatologies 113.

Lind, S., Ingvaldsen, R.B., 2012. Variability and impacts of Atlantic Water entering the Barents Sea from the north. Deep Sea Res. Part Oceanogr. Res. Pap. 62, 70–88. https://doi.org/10.1016/j.dsr.2011.12.007

Lundesgaard, Ø., Sundfjord, A., Renner, A.H.H., 2021. Drivers of Interannual Sea Ice Concentration Variability in the Atlantic Water Inflow Region North of Svalbard. J. Geophys. Res. Oceans 126, e2020JC016522. https://doi.org/10.1029/2020JC016522

Madec, Gurvan, 2008. NEMO ocean engine. Note du Pôle de modélisation, Institut Pierre-Simon Laplace (IPSL), France, No 27, ISSN No 1288-1619.

Menze, S., Ingvaldsen, R.B., Haugan, P., Fer, I., Sundfjord, A., Beszczynska-Moeller, A., Falk-Petersen, S., 2019. Atlantic Water Pathways Along the North-Western Svalbard Shelf Mapped Using Vessel-Mounted Current Profilers. J. Geophys. Res. Oceans 124, 1699–1716. https://doi.org/10.1029/2018JC014299

Meyer, A., Fer, I., Sundfjord, A., Peterson, A.K., 2017a. Mixing rates and vertical heat fluxes north of Svalbard from Arctic winter to spring. J. Geophys. Res. Oceans 4569–4586. https://doi.org/10.1002/2016JC012441@10.1002/(ISSN)2169-9291.NICE1

Meyer, A., Sundfjord, A., Fer, I., Provost, C., Robineau, N.V., Koenig, Z., Onarheim, I.H., Smedsrud, L.H., Duarte, P., Dodd, P.A., Graham, R.M., Schmidtko, S., Kauko, H.M., 2017b. Winter to summer oceanographic observations in the Arctic Ocean north of Svalbard. J. Geophys. Res. Oceans 122, 6218–6237. https://doi.org/10.1002/2016JC012391

Onarheim, I.H., Eldevik, T., Smedsrud, L.H., Stroeve, J.C., 2018. Seasonal and Regional Manifestation of Arctic Sea Ice Loss. J. Clim. 31, 4917–4932. https://doi.org/10.1175/JCLI-D-17-0427.1

752 Onarheim, I.H., Smedsrud, L.H., Ingvaldsen, R.B., Nilsen, F., 2014. Loss of sea ice during winter north
753 of Svalbard. Tellus Dyn. Meteorol. Oceanogr. 66, 23933.
754 https://doi.org/10.3402/tellusa.v66.23933
755 Pérez-Hernández, M.D., Pickart, R.S., Pavlov, V., Våge, K., Ingvaldsen, R., Sundfjord, A., Renner,
756 A.H.H., Torres, D.J., Erofeeva, S.Y., 2017. The Atlantic Water boundary current north of
757 Svalbard in late summer. J. Geophys. Res. Oceans 122, 2269–2290.
758 https://doi.org/10.1002/2016JC012486
759 Pérez-Hernández, M.D., Pickart, R.S., Torres, D.J., Bahr, F., Sundfjord, A., Ingvaldsen, R., Renner,
760 A.H.H., Beszczynska-Möller, A., Appen, W.-J. von, Pavlov, V., 2019. Structure, Transport, and
761 Seasonality of the Atlantic Water Boundary Current North of Svalbard: Results From a
762 Yearlong Mooring Array. J. Geophys. Res. Oceans 124, 1679–1698.
763 https://doi.org/10.1029/2018JC014759
764 Pickart, R.S., Moore, G.W.K., Torres, D.J., Fratantoni, P.S., Goldsmith, R.A., Yang, J., 2009. Upwelling
765 on the continental slope of the Alaskan Beaufort Sea: Storms, ice, and oceanographic
766 response. J. Geophys. Res. Oceans 114. https://doi.org/10.1029/2008JC005009
767 Polyakov, I.V., Alkire, M.B., Bluhm, B.A., Brown, K.A., Carmack, E.C., Chierici, M., Danielson, S.L.,
768 Ellingsen, I., Ershova, E.A., Gårdfeldt, K., Ingvaldsen, R.B., Pnyushkov, A.V., Slagstad, D.,
769 Wassmann, P., 2020a. Borealization of the Arctic Ocean in Response to Anomalous Advection
770 From Sub-Arctic Seas. Front. Mar. Sci. 7. https://doi.org/10.3389/fmars.2020.00491
771 Polyakov, I.V., Pnyushkov, A.V., Alkire, M.B., Ashik, I.M., Baumann, T.M., Carmack, E.C., Goszczko, I.,
772 Guthrie, J., Ivanov, V.V., Kanzow, T., Krishfield, R., Kwok, R., Sundfjord, A., Morison, J.,
773 Rember, R., Yulin, A., 2017. Greater role for Atlantic inflows on sea-ice loss in the Eurasian
774 Basin of the Arctic Ocean. Science 356, 285–291. https://doi.org/10.1126/science.aai8204
775 Polyakov, I.V., Rippeth, T.P., Fer, I., Alkire, M.B., Baumann, T.M., Carmack, E.C., Ingvaldsen, R., Ivanov,
776 V.V., Janout, M., Lind, S., Padman, L., Pnyushkov, A.V., Rember, R., 2020b. Weakening of Cold
777 Halocline Layer Exposes Sea Ice to Oceanic Heat in the Eastern Arctic Ocean. J. Clim. 33,
778 8107–8123. https://doi.org/10.1175/JCLI-D-19-0976.1
779 Polyakov, I.V., Rippeth, T.P., Fer, I., Baumann, T.M., Carmack, E.C., Ivanov, V.V., Janout, M., Padman,
780 L., Pnyushkov, A.V., Rember, R., 2020c. Intensification of Near-Surface Currents and Shear in
781 the Eastern Arctic Ocean. Geophys. Res. Lett. 47, e2020GL089469.
782 https://doi.org/10.1029/2020GL089469
783 Polyakov, I.V., Timokhov, L.A., Alexeev, V.A., Bacon, S., Dmitrenko, I.A., Fortier, L., Frolov, I.E.,
784 Gascard, J.-C., Hansen, E., Ivanov, V.V., Laxon, S., Mauritzen, C., Perovich, D., Shimada, K.,
785 Simmons, H.L., Sokolov, V.T., Steele, M., Toole, J., 2010. Arctic Ocean Warming Contributes
786 to Reduced Polar Ice Cap. J. Phys. Oceanogr. 40, 2743–2756.
787 https://doi.org/10.1175/2010JPO4339.1
788 Randelhoff, A., Sundfjord, A., 2018. Short commentary on marine productivity at Arctic shelf breaks:
789 upwelling, advection and vertical mixing. Ocean Sci. 14, 293–300.
790 https://doi.org/10.5194/os-14-293-2018
791 Renner, A.H.H., Sundfjord, A., Janout, M.A., Ingvaldsen, R.B., Beszczynska-Möller, A., Pickart, R.S.,
792 Pérez-Hernández, M.D., 2018. Variability and Redistribution of Heat in the Atlantic Water
793 Boundary Current North of Svalbard. J. Geophys. Res. Oceans 123, 6373–6391.
794 https://doi.org/10.1029/2018JC013814
795 Ricker, R., Kauker, F., Schweiger, A., Hendricks, S., Zhang, J., Paul, S., 2021. Evidence for an Increasing
796 Role of Ocean Heat in Arctic Winter Sea Ice Growth. J. Clim. 34, 5215–5227.
797 https://doi.org/10.1175/JCLI-D-20-0848.1
798 Rigor, I.G., Colony, R.L., Martin, S., 2000. Variations in Surface Air Temperature Observations in the
799 Arctic, 1979–97. J. Clim. 13, 896–914. https://doi.org/10.1175/1520-
800 0442(2000)013<0896:VISATO>2.0.CO;2
801 Rossow, W.B., Schiffer, R.A., 1999. Advances in Understanding Clouds from ISCCP. Bull. Am.
802 Meteorol. Soc. 80, 2261–2288. https://doi.org/10.1175/1520-
803 0477(1999)080<2261:AIUCFI>2.0.CO;2

804 Rousset, C., Vancoppenolle, M., Madec, G., Fichefet, T., Flavoni, S., Barthélemy, A., Benshila, R.,
805 Chanut, J., Lévy, C., Masson, S., Vivier, F., 2015. The Louvain-La-Neuve sea ice model LIM3.6:
806 global and regional capabilities. Geosci. Model Dev. 8, 2991–3005.
807 https://doi.org/10.5194/gmd-8-2991-2015
808 Rudels, B., Jones, E.P., Schauer, U., Eriksson, P., 2004. Atlantic sources of the Arctic Ocean surface
809 and halocline waters. Polar Res. 23, 181–208. https://doi.org/10.1111/j.1751-
810 8369.2004.tb00007.x
811 Sirevaag, A., Fer, I., 2009. Early Spring Oceanic Heat Fluxes and Mixing Observed from Drift Stations
812 North of Svalbard. J. Phys. Oceanogr. 39, 3049–3069.
813 https://doi.org/10.1175/2009JPO4172.1
814 Skagseth, Ø., Furevik, T., Ingvaldsen, R., Loeng, H., Mork, K.A., Orvik, K.A., Ozhigin, V., 2008. Volume
815 and Heat Transports to the Arctic Ocean Via the Norwegian and Barents Seas, in: Dickson,
816 R.R., Meincke, J., Rhines, P. (Eds.), Arctic–Subarctic Ocean Fluxes: Defining the Role of the
817 Northern Seas in Climate. Springer Netherlands, Dordrecht, pp. 45–64.
818 https://doi.org/10.1007/978-1-4020-6774-7_3
819 Spall, M.A., 2013. On the Circulation of Atlantic Water in the Arctic Ocean. J. Phys. Oceanogr. 43,
820 2352–2371. https://doi.org/10.1175/JPO-D-13-079.1
821 Steele, M., Morley, R., Ermold, W., 2001. PHC: A Global Ocean Hydrography with a High-Quality
822 Arctic Ocean. J. Clim. 14, 2079–2087. https://doi.org/10.1175/1520-
823 0442(2001)014<2079:PAGOHW>2.0.CO;2
824 Våge, K., Pickart, R.S., Pavlov, V., Lin, P., Torres, D.J., Ingvaldsen, R., Sundfjord, A., Proshutinsky, A.,
825 2016. The Atlantic Water boundary current in the Nansen Basin: Transport and mechanisms
826 of lateral exchange. J. Geophys. Res. Oceans 121, 6946–6960.
827 https://doi.org/10.1002/2016JC011715
828 Yeager, S.G., Karspeck, A.R., Danabasoglu, G., 2015. Predicted slowdown in the rate of Atlantic sea
829 ice loss. Geophys. Res. Lett. 42, 10,704-10,713. https://doi.org/10.1002/2015GL065364
830

831

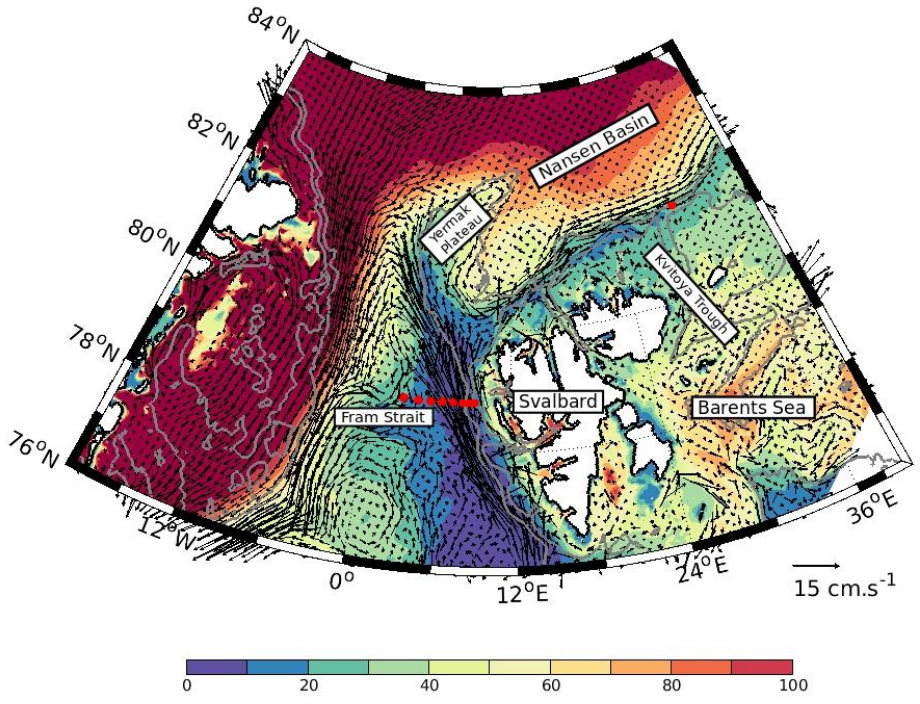

Figure 1: Simulated winter (December-March) velocity at 60 m depth (arrows) and depth (m) of the 0°C isotherm (color) averaged over the 1997-2017 period. The red dots indicate the positions of the moorings which were used for the model-observation comparison (see supporting information).

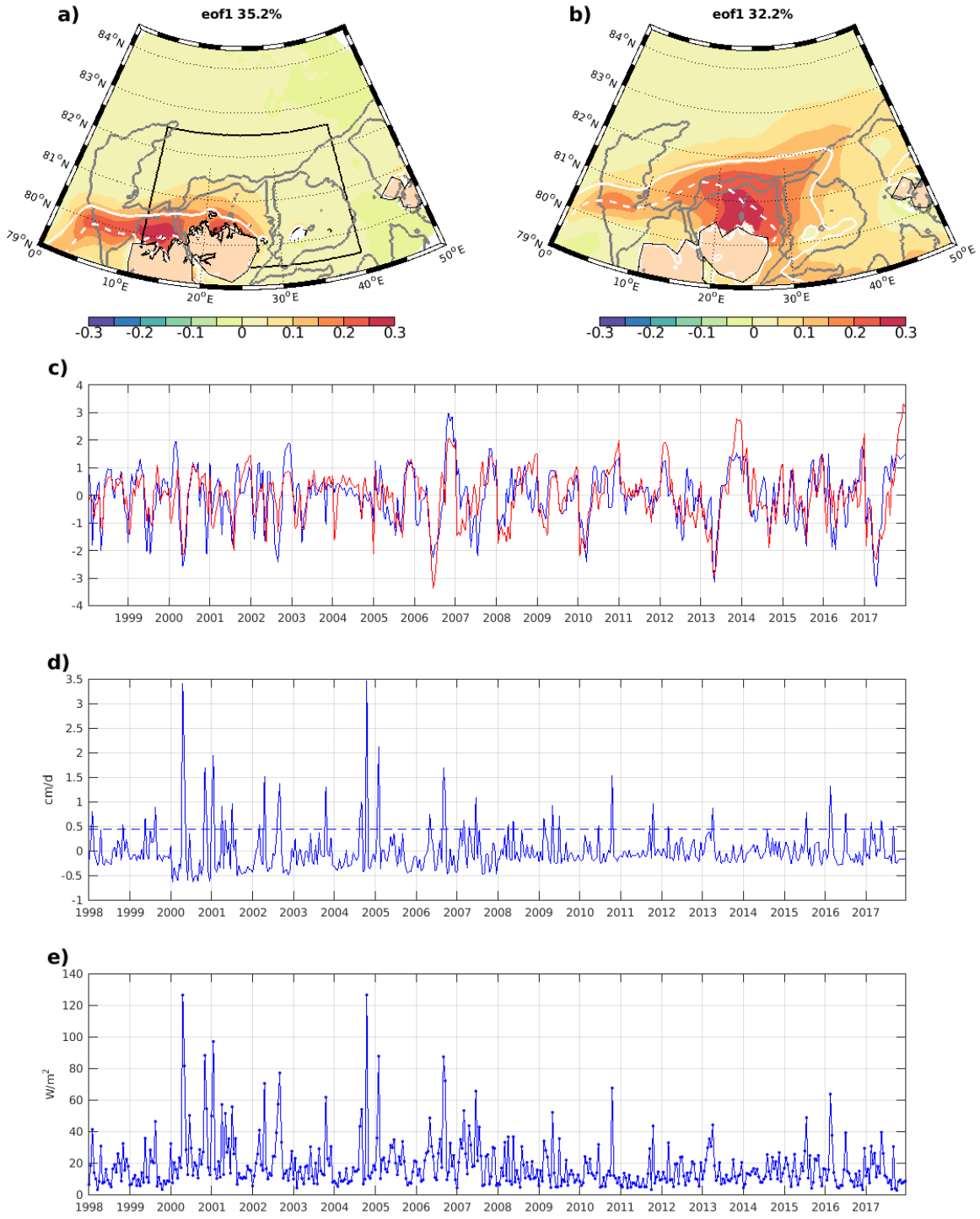

Figure 2: (a)-(b) Loading patterns of the first EOF mode of the winter (DJFM) SIC in (a) the model simulation and (b) the observations. (c) Normalized Principal Component associated with the first EOF mode of the (blue) simulated and (red) observed winter SIC. SIC anomalies are constructed by removing the mean of each winter. (d) Melt index (see definition in text) with its standard deviation (dashed line). (e) Ice-ocean heat flux (W m^{-2}, positive values indicate upward fluxes) averaged over the study area (shown as a black box in (a)). Also shown in (a) and (b) are the 250 m and 1000 m isobaths (grey), the 50% (dashed white contour) and 80% (solid white contour) isopleths of mean winter SIC.

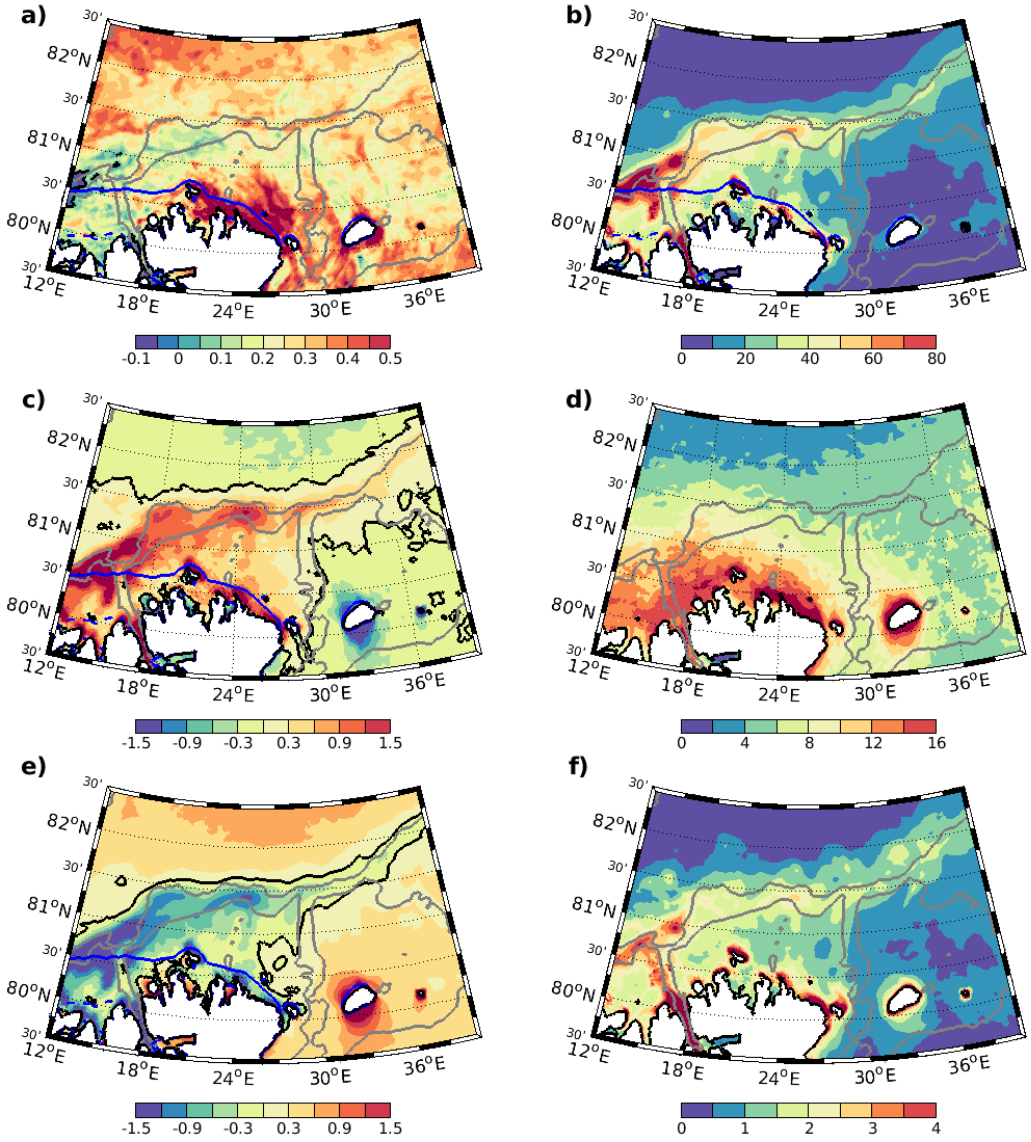

Figure 3: Left panels: Simulated mean winter (DJFM) ice volume change (cm day^{-1}): (a) net volume change and the contributions from (c) the ice volume transport convergence and (e) the net thermodynamic growth. Right panels: (b) ice-ocean heat flux (W m^{-2}, positive values indicate upward fluxes), (d) standard deviation of the ice volume transport convergence (cm day^{-1}) and (f) standard deviation of the net thermodynamic growth (cm day^{-1}). Standard deviations calculated over all winters of the simulation. Also shown in (a), (b) (c), and (e) are the 50% (dashed blue) and 80% (solid blue) isopleths of the mean winter SIC. Grey contours represent the 250 m and 1000 m isobaths. The black contour in (c) and (e) represents the 0 isopleth.

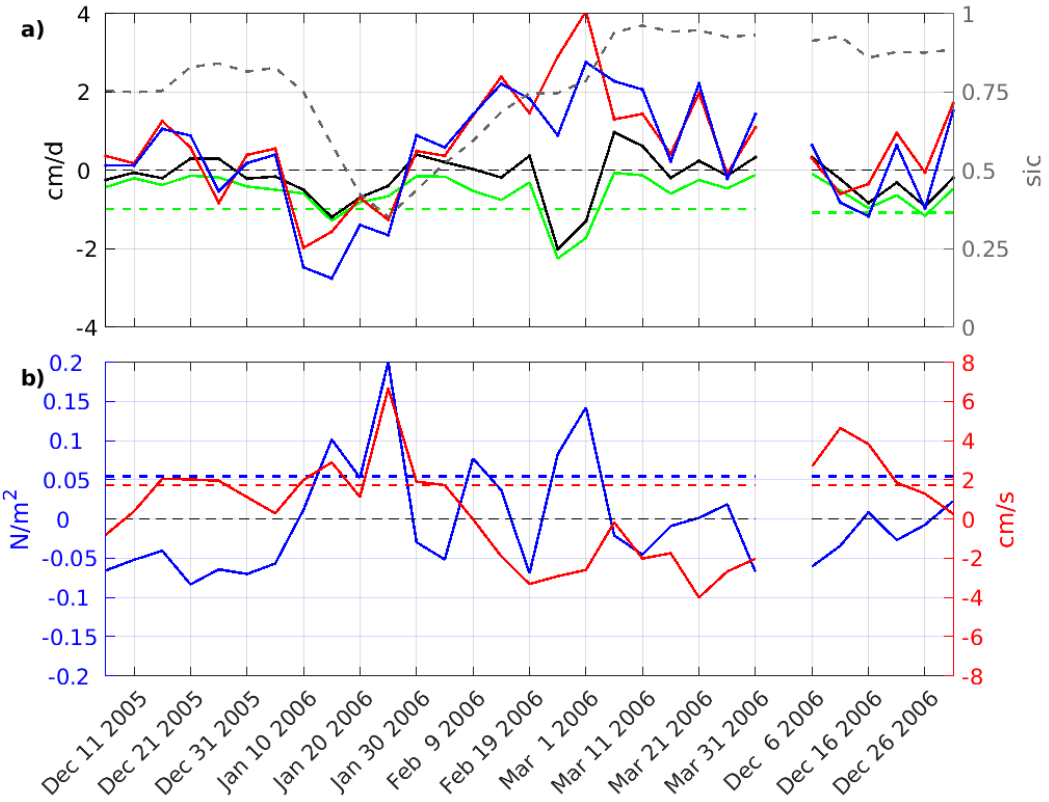

Figure 4: (a) 5-day ice volume change (cm day^{-1}) averaged over the study area over 2005-2006: net volume change (blue) and the part contributed by subregions of net ice melt (solid green), contributions from the ice volume transport convergence (red) and the thermodynamic ice growth (black). Also shown in (a) are, the limit on the mean winter melt rate for identification of large melt events (dashed green) and the SIC averaged over the study area (dashed grey). (b) Surface stress index (blue) and boundary current index (red), with their limits for identification of large stress events (dashed blue) and strong current events (dashed red), respectively (see sections 3.4.2.2 and 3.4.2.3 for the definition of the indices).

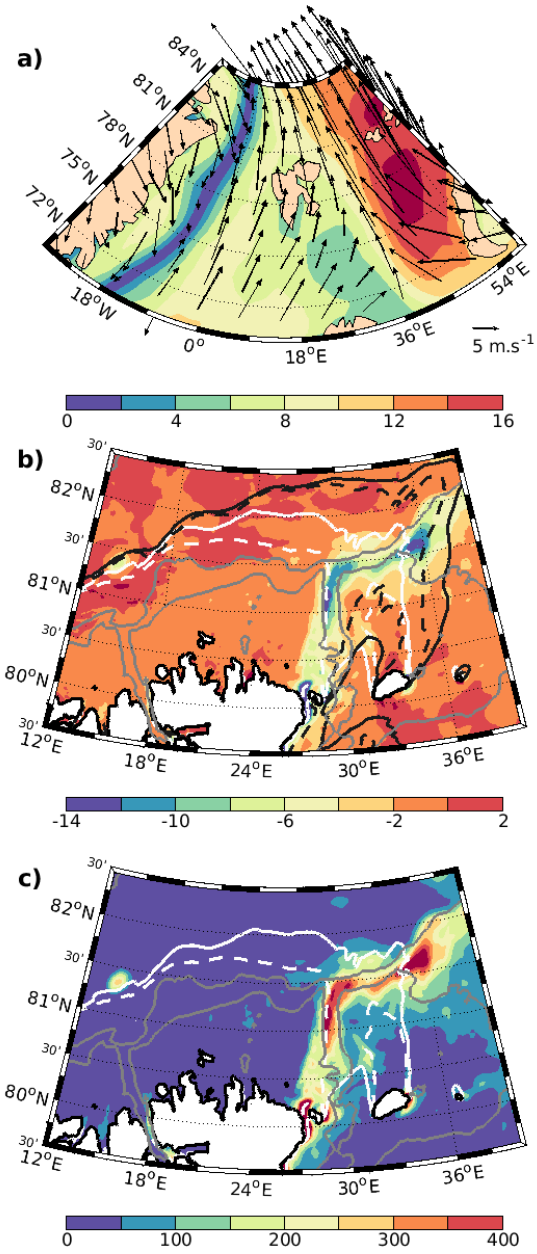

Figure 5: (a) 10 m wind vector (arrows) and wind speed (m s^{-1}) (color), (b) thermodynamic ice growth (cm day^{-1}) and (c) ice-ocean heat flux (W m^{-2}, positive values indicate upward fluxes) on January 15, 2006. The 50% (dashed line) and 80% (solid line) SIC isopleths are also shown in (b) and (c) for January 15, 2006 (white) and in (b) for January 20, 2006 (black). Grey contours represent the 250 m and 1000 m isobaths.

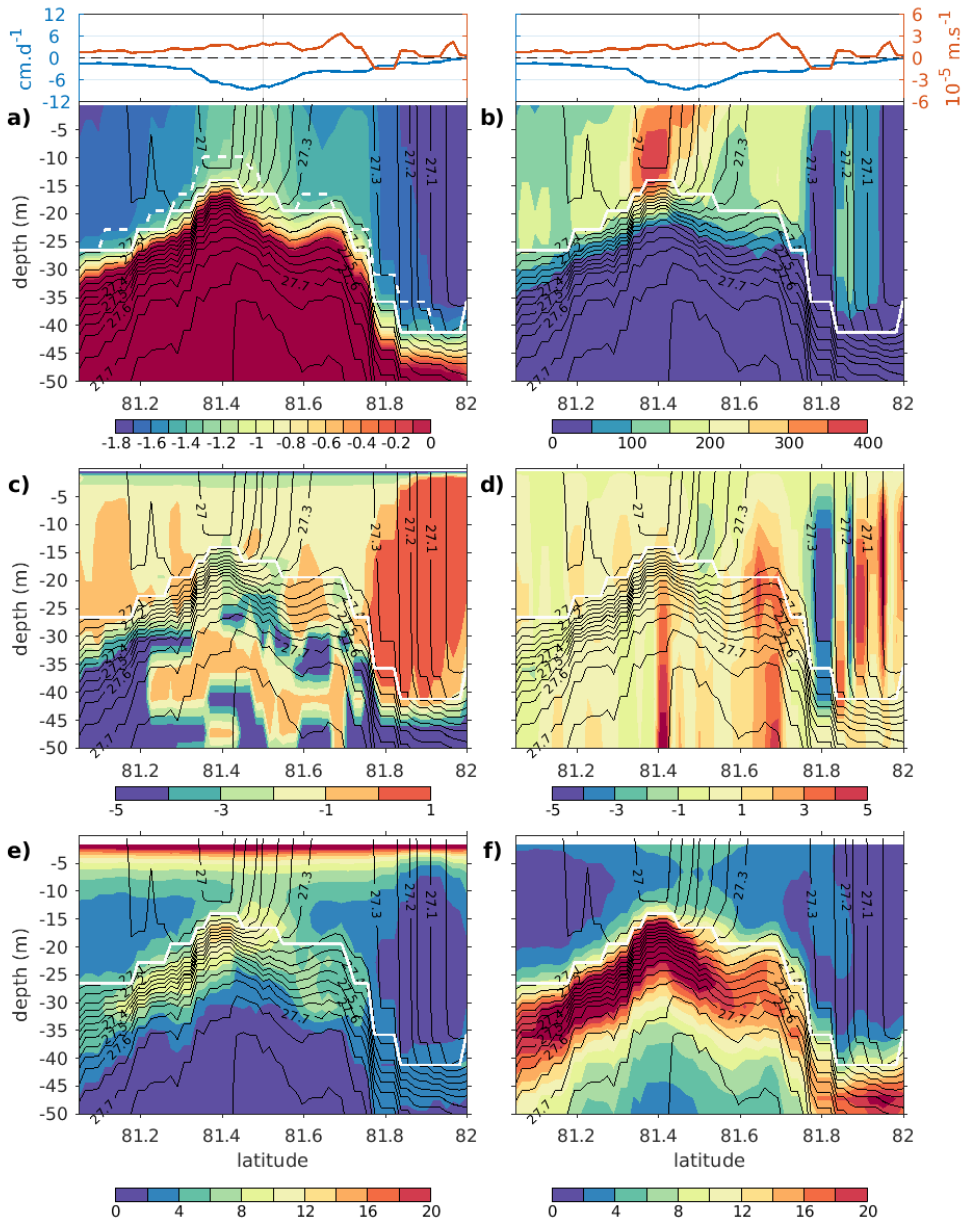

Figure 6: (a) Temperature (°C), (b) vertical diffusive heat flux (W m^{-2}, positive values indicate upward fluxes), (c) vertical diffusion coefficient (m^2 s^{-1}) expressed as $\log_{10}(K_v)$, (d) vertical velocity (10^{-5} m s^{-1}), (e) velocity shear (10^{-3} s^{-1}), and (f) Brunt Väisälä frequency (10^{-3} s^{-1}) on a meridional section along 31°E on January 15, 2006. On top panels are shown the thermodynamic ice growth (cm day^{-1}, blue) and the Ekman pumping velocity (10^{-5} m s^{-1}, red). The mixed layer depth is shown as a white line in all panels for January 15 (solid) and in (a) for January 10 (dashed).

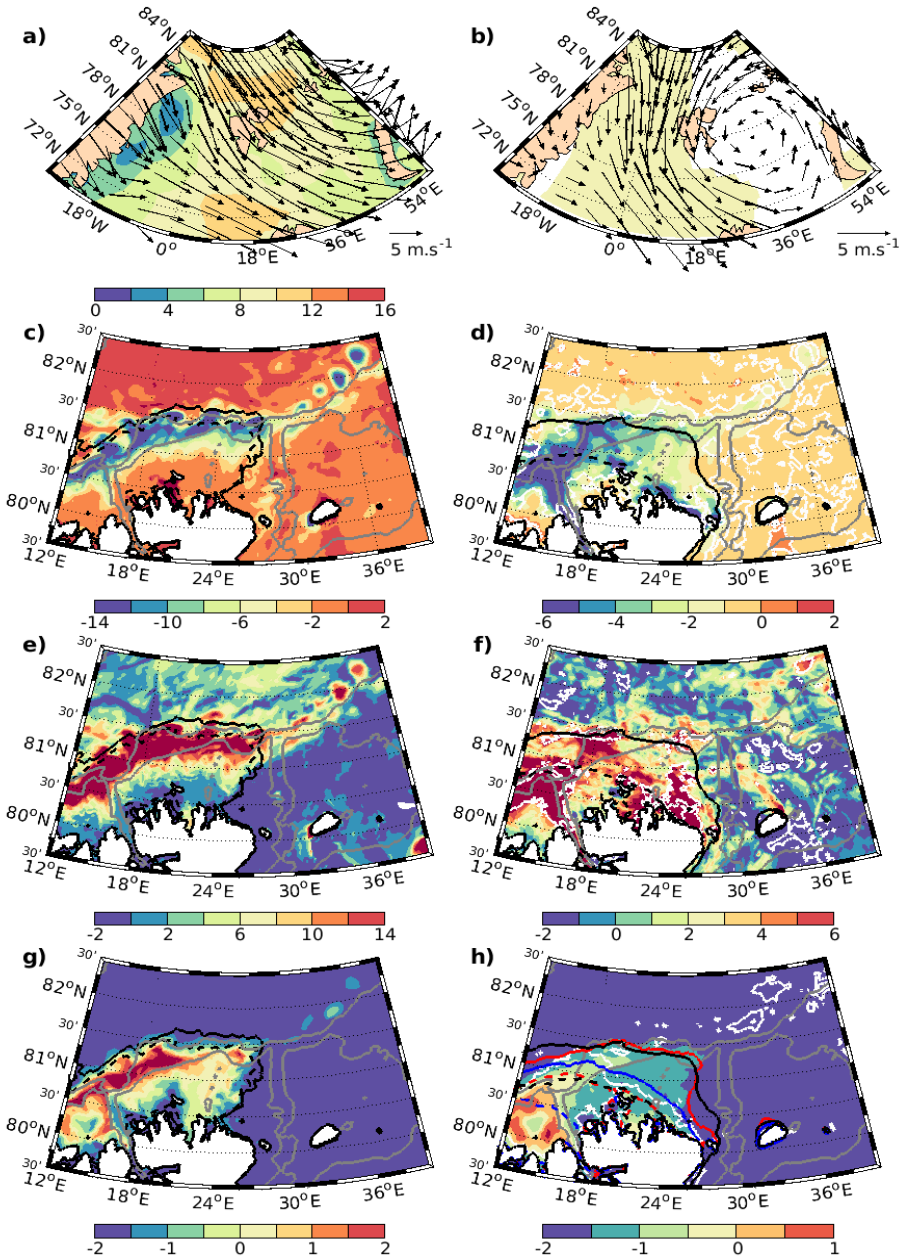

Figure 7: Left panels: (a) 10 m wind (arrow) and wind speed (m s^{-1}) (color), (c) thermodynamic ice growth (cm day^{-1}), and (e) ice volume transport convergence (cm day^{-1}) on February 24, 2006. (g) SST (°C) on February 19, 2006. Also shown in (c)-(g) as black contours are the 50% (dashed) and 80% (solid) SIC isopleths on February 24. Right panels: (b, d, f) Composite difference between large melt events associated with ice advection over warm SST and other events for (b) the 10 m wind, (d) the thermodynamic ice growth (cm day^{-1}), (f) the ice volume transport convergence (cm day^{-1}). Also shown in (d) and (f) as black lines are the 50% (dashed) and 80% (solid) SIC isopleths averaged over these large melt events. (h) composites of the SST (°C) five days prior to the large melt events. Also plotted in (h) are the 50% (dashed) and 80% (solid) SIC isopleths 5 days before (red), in phase (black) and 5 days after (blue) the large melt events. The area of 95% confidence level for the composites is delimited by yellow shading in (b) and white lines in (d), (f) and (h). Grey contours represent the 250 m and 1000 m isobaths.

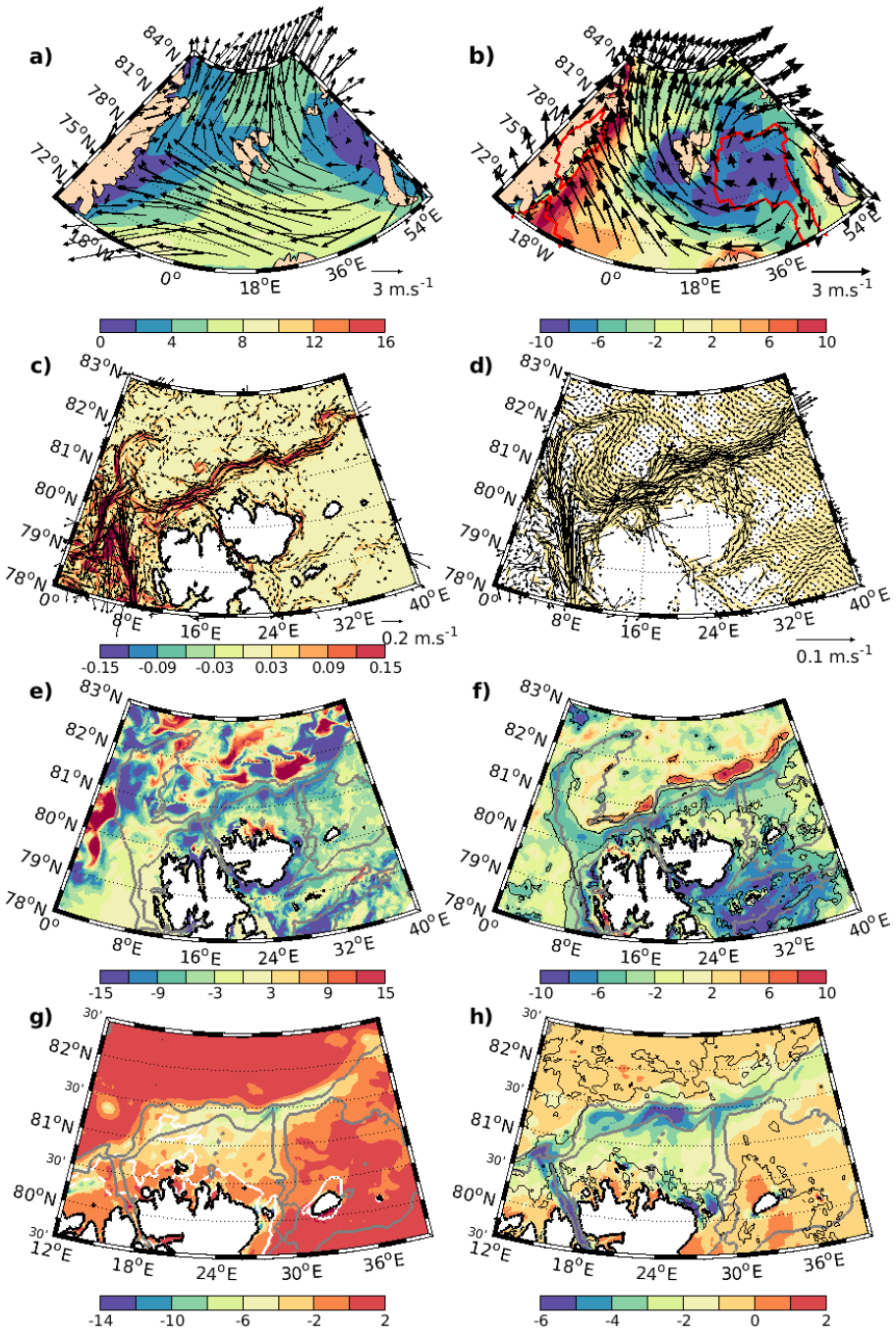

Figure 8: Left panels: (a) 10 m wind (arrows) and wind speed (m s^{-1}, color shading) and (g) thermodynamic ice growth (cm day^{-1}) on December 26, 2006. (c) current velocity anomaly (arrows) and velocity speed anomaly (m s^{-1}, color shading) averaged between 20 and 40 meters and (e) anomaly of the depth (m) of the 0°C isotherm, on December 11, 2006. The 50% (dashed white line) and 80% (solid white line) SIC isopleths are also shown in (g). Right panels: Composites of anomalies of (b) the 10 m wind (arrows) and surface wind curl (10^{-6} s^{-1}, color shading), (d) the current velocity averaged between 20 and 40 m and (f) the depth (m) of the 0°C isotherm, for the strong current events, (h) composites of anomalies of the thermodynamic ice growth (cm day^{-1}) for large melt events associated with strong current. All anomalies are calculated relative to the winter average.

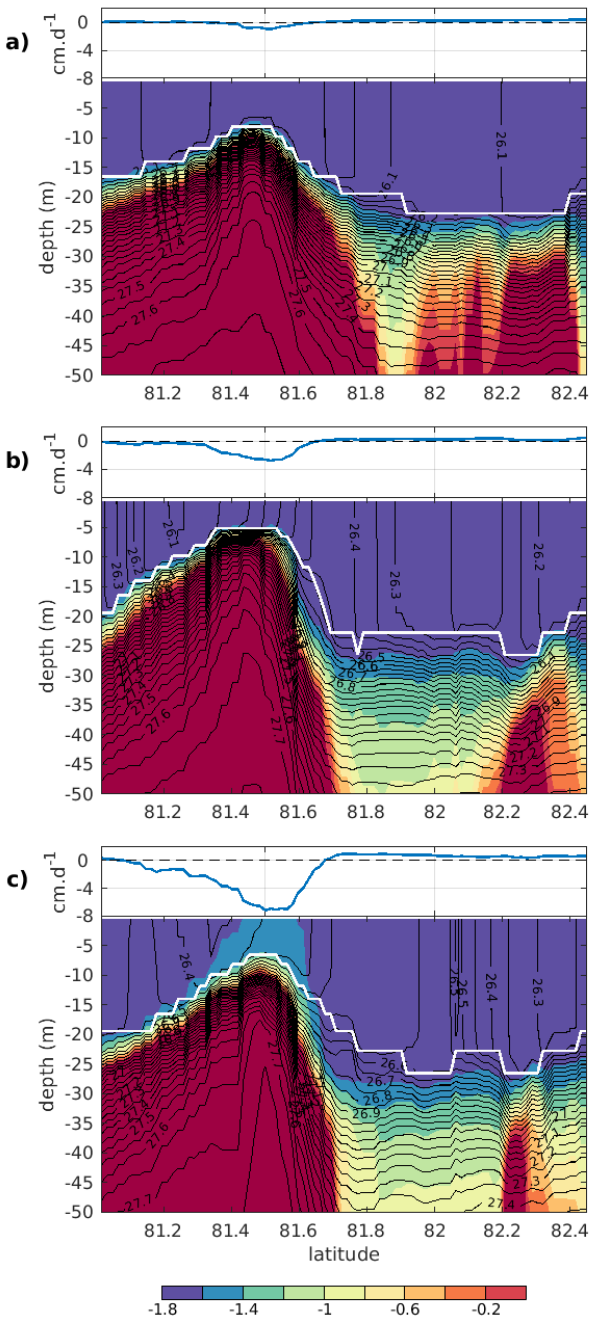

911

912 Figure 9: Temperature (°C, color shading) and density (sigma units, black contours) overlaid
913 with the mixed layer depth (white line) on a meridional section along 31°E on (a) December 1,
914 (b) December 16 and (c) December 26, 2006. On top of each panel, the thermodynamic ice
915 growth rate along the section is also plotted.

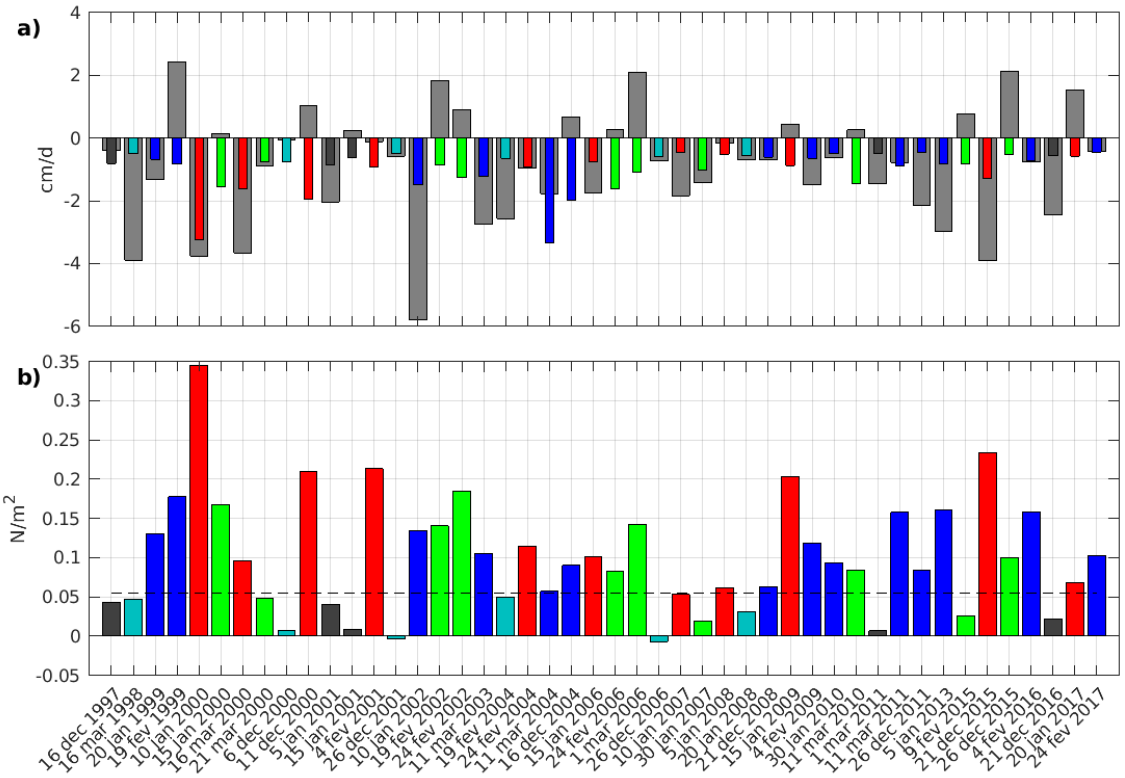

Figure 10: (a) ice volume change (cm day^{-1}) averaged over the study area for all the large melt events (grey bar), overlaid with the ice melt contribution (narrow bar) for those large melt events only associated with large stress (blue), ice advection over warm SST (green), large stress and strong current (red), and large current (cyan). Large melt events which are not associated with any specific process are shown in black. (b) surface stress (N m^{-2}) averaged over the study area with same color code for the different types of large melt events defined in (a), and its standard deviation (dashed line).

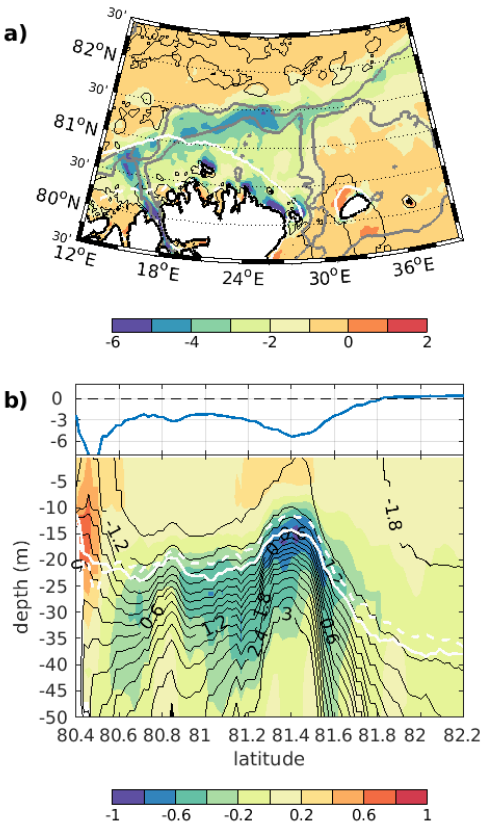

Figure 11: (a) Composite difference of the thermodynamic ice growth (cm day^{-1}) between the large melt events associated with large stress and other melt events. (b) Composites of the temperature (°C, black contours) for the large melt events associated with large stress and the difference between the in-phase temperature and the temperature 5 days prior to these events (°C, color shading) on a meridional section along 24°E. Also shown as white lines in (a) are the 50% (dashed) and 80% (solid) isopleths of the SIC averaged over these large melt events and in (b) is the mixed layer depth in phase with (solid) and five days prior to (dashed) the melt event. On top of (b), the thermodynamic ice growth rate (cm day^{-1}) is shown along the section.

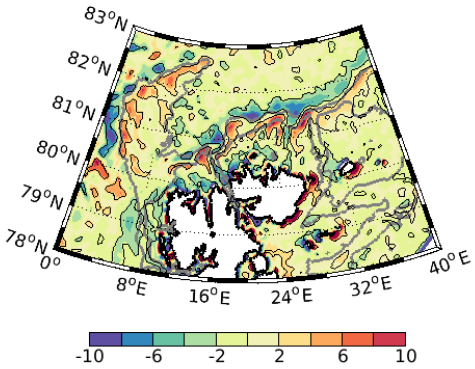

Figure 12: Composites of anomalies of the Ekman suction velocity (10^{-6} m s^{-1}) for the strong current events. Anomalies are calculated relative to the winter average.

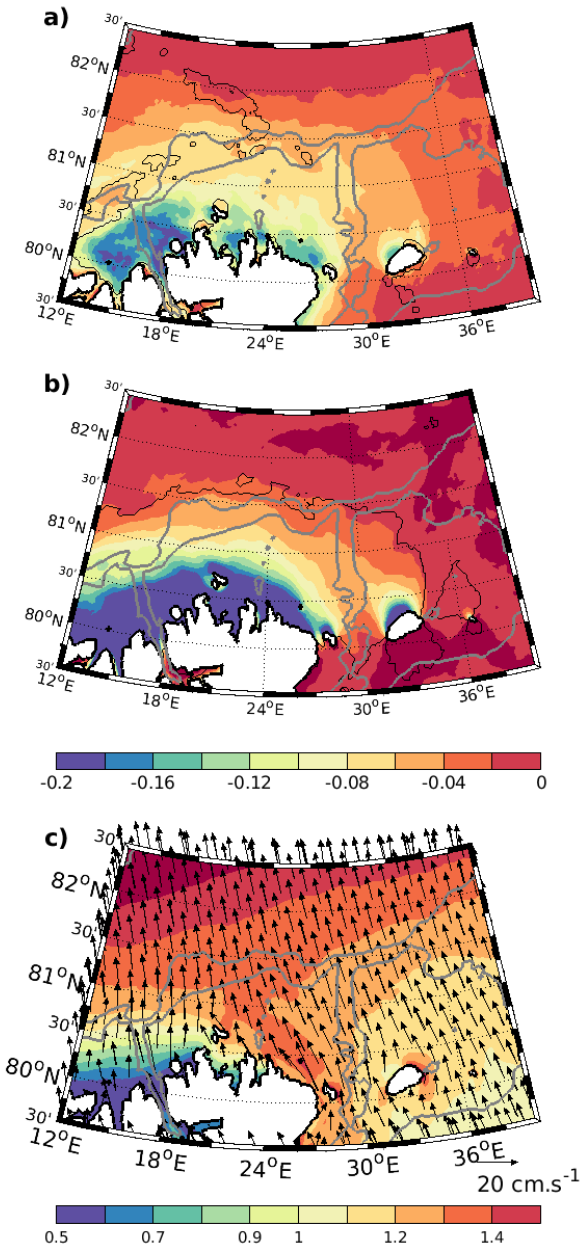

Figure 13: Composites of the SIC change between two consecutive 5-day periods for (a) the large melt events and (b) the events of large ice volume transport divergence. (c) Composites of the ice drift anomalies (arrows) superimposed on the mean winter ice thickness (m, color shading) for events of large ice volume transport divergence. In (a) and (b) the thin black line represents the 95% confidence level for the composites. Grey contours represent the 250 m and 1000 m isobaths.